

Integrative *in situ* mapping of single-cell transcriptional states and tissue histopathology in a mouse model of Alzheimer's disease

Received: 29 August 2021

Accepted: 20 December 2022

Published online: 2 February 2023

Hu Zeng^{1,2,7}, Jiahao Huang  , Haowen Zhou^{1,7}, William J. Meilandt³, Borislav Dejanovic  , Yiming Zhou^{1,2}, Christopher J. Bohlen³, Seung-Hye Lee³, Jingyi Ren^{1,2}, Albert Liu², Zefang Tang^{1,2}, Hao Sheng  , Jia Liu  , Morgan Sheng   & Xiao Wang  

 Check for updates

Complex diseases are characterized by spatiotemporal cellular and molecular changes that may be difficult to comprehensively capture. However, understanding the spatiotemporal dynamics underlying pathology can shed light on disease mechanisms and progression. Here we introduce STARmap PLUS, a method that combines high-resolution spatial transcriptomics with protein detection in the same tissue section. As proof of principle, we analyze brain tissues of a mouse model of Alzheimer's disease at 8 and 13 months of age. Our approach provides a comprehensive cellular map of disease progression. It reveals a core–shell structure where disease-associated microglia (DAM) closely contact amyloid- β plaques, whereas disease-associated astrocyte-like (DAA-like) cells and oligodendrocyte precursor cells (OPCs) are enriched in the outer shells surrounding the plaque-DAM complex. Hyperphosphorylated tau emerges mainly in excitatory neurons in the CA1 region and correlates with the local enrichment of oligodendrocyte subtypes. The STARmap PLUS method bridges single-cell gene expression profiles with tissue histopathology at subcellular resolution, providing a tool to pinpoint the molecular and cellular changes underlying pathology.

Alzheimer's disease (AD) is a progressive neurodegenerative disorder and the most common cause of dementia in the elderly¹. Widespread deposition of extracellular amyloid- β (A β) plaques and intracellular neurofibrillary tangles (hyperphosphorylated tau deposits), especially in the neocortex and hippocampus, are the neuropathologic hallmarks

of AD^{1–4}. In addition, AD pathology is characterized by reactive changes of microglia and astrocytes and white matter abnormalities^{5–7}. A key question in AD research is how these histopathological hallmarks are correlated with molecular disturbances that drive neurodegeneration across different cell populations.

¹Broad Institute of MIT and Harvard, Cambridge, MA, USA. ²Department of Chemistry, Massachusetts Institute of Technology, Cambridge, MA, USA.

³Department of Neuroscience, Genentech, Inc., South San Francisco, CA, USA. ⁴Stanley Center for Psychiatric Research, Broad Institute of MIT and

Harvard, Cambridge, MA, USA. ⁵John A. Paulson School of Engineering and Applied Sciences, Harvard University, Boston, MA, USA. ⁶Department of

Brain and Cognitive Sciences, Massachusetts Institute of Technology, Cambridge, MA, USA. ⁷These authors contributed equally: Hu Zeng, Jiahao Huang,

Haowen Zhou.  e-mail: msheng@broadinstitute.org; wangxiao@broadinstitute.org

Conventional experimental approaches have limitations in uncovering the molecular and cellular complexity of AD as follows: bulk-tissue analyses mask the heterogeneity of cell populations in the brain, and standard imaging methods visualize only a few genes/proteins and access limited cell types. The recent application of single-cell RNA sequencing (scRNA-seq) to AD brain tissue has been transformative, revealing substantial and heterogeneous changes of gene expression in major brain cell types in patients and mouse models^{8–13}. A subpopulation of microglia with a distinctive transcriptomic state (termed disease-associated microglia or DAM) was identified by bulk and scRNA-seq studies in mouse models of AD and other neurodegenerative disorders^{10,14–19}. Besides DAM microglia, there are also reactive astrocytes, such as disease-associated astrocytes (DAA), with characteristic gene signatures in AD patients and mouse models, suggesting a major transcriptional response in AD by multiple cell types^{9,20–25}.

However, there are major limitations of scRNA-seq methods: they cannot preserve the spatial pattern of individual cells, or their spatial relationships to localized tissue pathology, and the isolation of single cells or single nuclei from the brain tissue can introduce significant bias in cellular representation and artificial changes in gene expression, especially for microglia^{26–29}. Therefore, an advanced technology platform capable of integrating spatially resolved single-cell transcriptomics with histology and immunostaining in intact tissue is needed to fully understand the scope and heterogeneity of diverse cellular responses to amyloid plaque, tau aggregation, cell death and synapse loss and to investigate the spatial relationships between the above-localized pathologies and cellular responses.

Spatially resolved transcriptomic technologies are capable of mapping transcriptomic profiles within tissue architecture^{30–37}, but many existing ones are incompatible with protein detection in the same tissue sections or limited by spatial resolution and/or gene coverage. For example, a recent study uncovered amyloid plaque-induced genes (PIGs) using spatial transcriptomics with fluorescent staining of adjacent brain sections to correlate the positions of plaques with local gene expression³⁸. However, the resolution was limited to 100 μm and only a small set of genes were examined at cellular resolution.

We previously developed an image-based *in situ* RNA sequencing method called STARmap (spatially resolved transcript amplicon readout mapping) for single-cell transcriptional state profiling in three-dimensional (3D) intact brain tissues³⁴. Here we introduce STARmap with protein localization and unlimited sequencing (STARmap PLUS), enabling simultaneous high-resolution spatial transcriptomics concomitantly with specific protein localization in the same tissue section. In this study, we employed STARmap PLUS to draw a comprehensive transcriptomic atlas of AD at a voxel size of 95 × 95 × 350 nm across all brain cell types during the development of amyloid plaque and tau pathology, using TauPS2APP triple transgenic mice, an established AD mouse model that exhibits both amyloid plaque and tau pathologies (Fig. 1a). TauPS2APP mice express mutant forms of hPresenilin 2 (PS2), hAPP and h-tau, showing age-related brain amyloid deposition, tauopathy, neuroinflammation, neurodegeneration and cognitive deficits^{39,40}.

Fig. 1 | Simultaneous mapping of cell types, single-cell transcriptional states and tissue histopathology by STARmap PLUS. a, Overview of STARmap PLUS, an integrative *in situ* method, capable of simultaneously mapping thousands of RNA species and protein disease markers in the same intact 3D tissue at subcellular resolution. **b**, Schematics of STARmap PLUS. After the brain tissue is retrieved and fixed, the intracellular mRNAs are targeted by a pair of SNAIL (specific amplification of nucleic acids via intramolecular ligation) probes, which are then enzymatically ligated and amplified to generate amine-modified cDNA amplicons *in situ*. Meanwhile, protein markers are labeled with primary antibodies. Next, tissues with amine-modified cDNA amplicons, proteins and primary antibodies are modified by acrylic acid N-hydroxysuccinimide ester (AA-NHS) and copolymerized with acrylamide to generate a hydrogel-tissue hybrid that fixes the locations of biomolecules for *in situ* mapping. Each cDNA amplicon contains a gene-specific identifier sequence (orange) that can be

By mapping a targeted list of 2,766 genes, we created a high-resolution spatial cell atlas of 8- and 13-month-old TauPS2APP mouse brains in the context of extracellular Aβ plaques and intracellular hyperphosphorylated tau accumulation. Single-cell spatial transcriptomic analysis identified disease-associated gene pathways across diverse cell types in the cortical and hippocampal regions of the TauPS2APP model in comparison with control samples. Integrating the spatial maps of diverse cell types and states at different disease stages, we propose a comprehensive spatiotemporal model of AD disease progression. These studies provide important tools and resources for mechanistic understandings of AD and other neurodegenerative diseases at cellular and molecular levels.

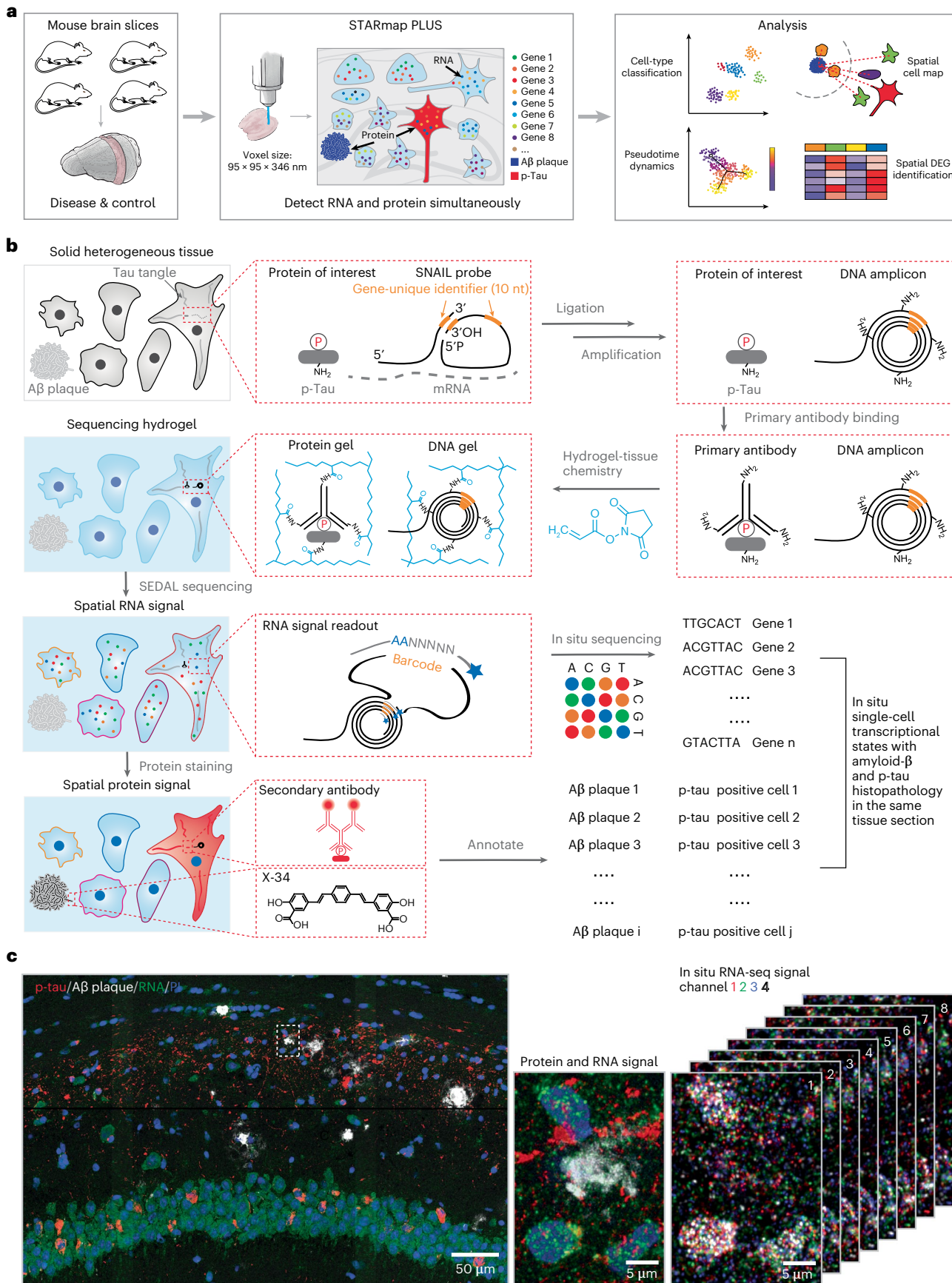
Results

Method development of STARmap PLUS

The original STARmap method is incompatible with histological staining (immunostaining or chemical staining) and limited to detecting 1,024 genes³⁴. To overcome such limitations, in STARmap PLUS, we developed the experimental protocol to incorporate antibody staining (in this study, AT8 antibody, detecting hyperphosphorylated tau) and dye staining (X-34, detecting Aβ plaque) into the library preparation and *in situ* sequencing steps (Fig. 1a,b and Extended Data Fig. 1a,b). In brief, STARmap PLUS entails the following steps: (1) mRNAs within fixed brain sections are detected by a pair of SNAIL (specific amplification of nucleic acids via intramolecular ligation) probes (Fig. 1b), and enzymatically amplified as cDNA amplicons; (2) specific proteins of interest are labeled with primary antibody; (3) the cDNA amplicons, primary antibodies and endogenous proteins (for example, plaques and tau) are chemically modified and copolymerized in a hydrogel matrix; (4) each cDNA amplicon contains a gene-unique identifier (barcode) that is readout through *in situ* sequencing with error reduction by dynamic annealing and ligation (SEDAL); (5) fluorescent secondary antibody and small-molecule dye X-34 are then applied to visualize specific proteins and their localization. Besides protein labeling capability, we expanded the gene-coding barcode in the DNA probes from 5 to 10 nucleotides (resulting in 10⁶ coding capacity for STARmap PLUS) that is sufficient to encode more than 20,000 genes (Fig. 1b). Notably, the tissue structure and histopathological morphology were well preserved after STARmap PLUS (Extended Data Fig. 1c,d). Furthermore, STARmap PLUS has superior detection efficiency in comparison with previously reported *in situ* sequencing methods^{37,41} (Extended Data Fig. 1e–h). In addition, STARmap PLUS is capable of detecting mRNAs and proteins in the same samples and has a much higher spatial resolution (95 × 95 × 350 nm voxel size) in comparison with chip-based spatial transcriptomics method (100 μm pixel size) that has been used previously in AD study³⁸.

We applied STARmap PLUS to investigate how AD-related pathology, particularly amyloid deposits and hyperphosphorylated tau, influences brain cell states at the transcriptomic level at subcellular resolution in intact brain tissue in which the spatial relationships between protein pathology, cell body location and mRNA changes are

readout through *in situ* sequencing with error reduction by dynamic annealing and ligation (SEDAL). Lastly, fluorescent protein stainings (secondary antibody and small-molecule dye X-34 stainings) were applied to visualize protein signals. **c**, Representative images showing the simultaneous mapping of cell nuclei, cDNA amplicons and protein signals in the brain slice from a 13-month-old TauPS2APP mouse. Left: The 3D projection of the raw confocal fluorescence image of the CA1 region of the hippocampus. Middle: A zoom-in view of the dashed box in the left panel, which shows the last cycle of tissue histopathology imaging that detects both protein and cDNA amplicon: red, immunofluorescent staining of p-tau; white, X-34 staining of Aβ plaque; green, fluorescent DNA probe staining of all cDNA amplicons; and blue, PI staining of cell nuclei. Right: eight cycles of *in situ* RNA sequencing of the view in the middle panel; each color represents a fluorescent channel in one round of *in situ* sequencing.



precisely maintained and readily measured. A curated list of 2,766 genes was extracted from previous bulk and single-cell RNA-seq studies and various AD-related databases (Supplementary Table 1)^{8,9,12,13,42–47}. We performed eight rounds of *in situ* sequencing to map RNAs and one round of postsequencing imaging to locate A β plaques and hyperphosphorylated tau (p-tau) in coronal sections of the brains from TauPS2APP mice and control mice (Fig. 1c and Extended Data Fig. 2a).

Transgenic TauPS2APP mice develop progressive amyloid plaques starting at ~4.5 months of age, growing exponentially from 6 months to 8 months of age, and rising steadily from 9 months of age. Neuronal damage, measured by disintegrative staining or volumetric MRI, becomes apparent by 9 months^{39,40}. Thus, brain sections were collected and analyzed at 8 months (when tau and A β pathology have set and are expanding) and 13 months (a more advanced disease stage with severe pathology and highly elevated neuroinflammatory activity)⁴⁰. We focused our spatial transcriptomic analysis on the retrosplenial cortex (RSP), the secondary motor cortex (MOs), the primary motor cortex (MOp), the primary somatosensory cortex (SSp) and the hippocampus. These regions contain plentiful plaques and are thus amenable to this kind of spatial analysis relative to plaque location. STARmap PLUS revealed that A β plaques were prominent in cortex and hippocampus, whereas AT8 p-tau immunoreactivity was strongest in the CA1 region of the hippocampus (Fig. 1c and Extended Data Fig. 2a), which is consistent with previous reports^{39,40}. A total of 38,788 cells from four TauPS2APP mice and 38,059 cells from four control mice (nontransgenic littermates) were imaged at a voxel size of 95 \times 95 \times 350 nm (Fig. 1a). After projecting 3D RNA reads to two-dimensional (2D) planes, segmenting cells and filtering single-cell transcriptional profiles by quality control criteria (Extended Data Fig. 2b; Methods), the remaining 72,165 cells pooled from all eight samples were subjected to downstream analysis (Extended Data Fig. 2b–g).

Hierarchical cell classification and spatial analysis

To identify cell types from the STARmap PLUS data, we adopted a hierarchical clustering strategy, where top-level clustering served to classify cells into common cell types shared by all samples, and sublevel clustering served to further identify disease-associated subtypes. During top-level clustering, the Leiden algorithm was applied to the k-Nearest Neighbors (kNN) graph constructed with the single-cell transcriptomic profiles after dimensionality reduction using principal component analysis (PCA). We identified 13 major clusters and annotated the cell types according to their spatial distribution and previously reported gene markers^{44,45,47} (Fig. 2a and Extended Data Fig. 3a). For example, excitatory neurons were annotated by their high expression levels of genes related to ion channels and synaptic signaling, such as *Vsnl1*, *Snap25* and *Dnm1*. Inhibitory neurons were separated by their enrichment of γ -aminobutyric acid transporter *Slc6a1*. Other non-neuronal cell-type-specific markers such as *Aldoc* for astrocyte, *Bsg* for endothelial cell, *Ctss* for microglia and *Plp1* for oligodendrocyte were used to annotate corresponding clusters (Extended Data Fig. 3a,b). The uniform manifold approximation and projection (UMAP) plots of TauPS2APP

samples showed differential distribution of cells within the astrocyte, microglia and oligodendrocyte clusters in comparison with controls, suggesting possible disease-associated cell subtypes (Fig. 2a and Extended Data Fig. 3c). Thus, we further investigated the transcriptomic heterogeneity within each major cell type, which further identified 33 sublevel clusters based on their transcriptomic signatures (Fig. 2b).

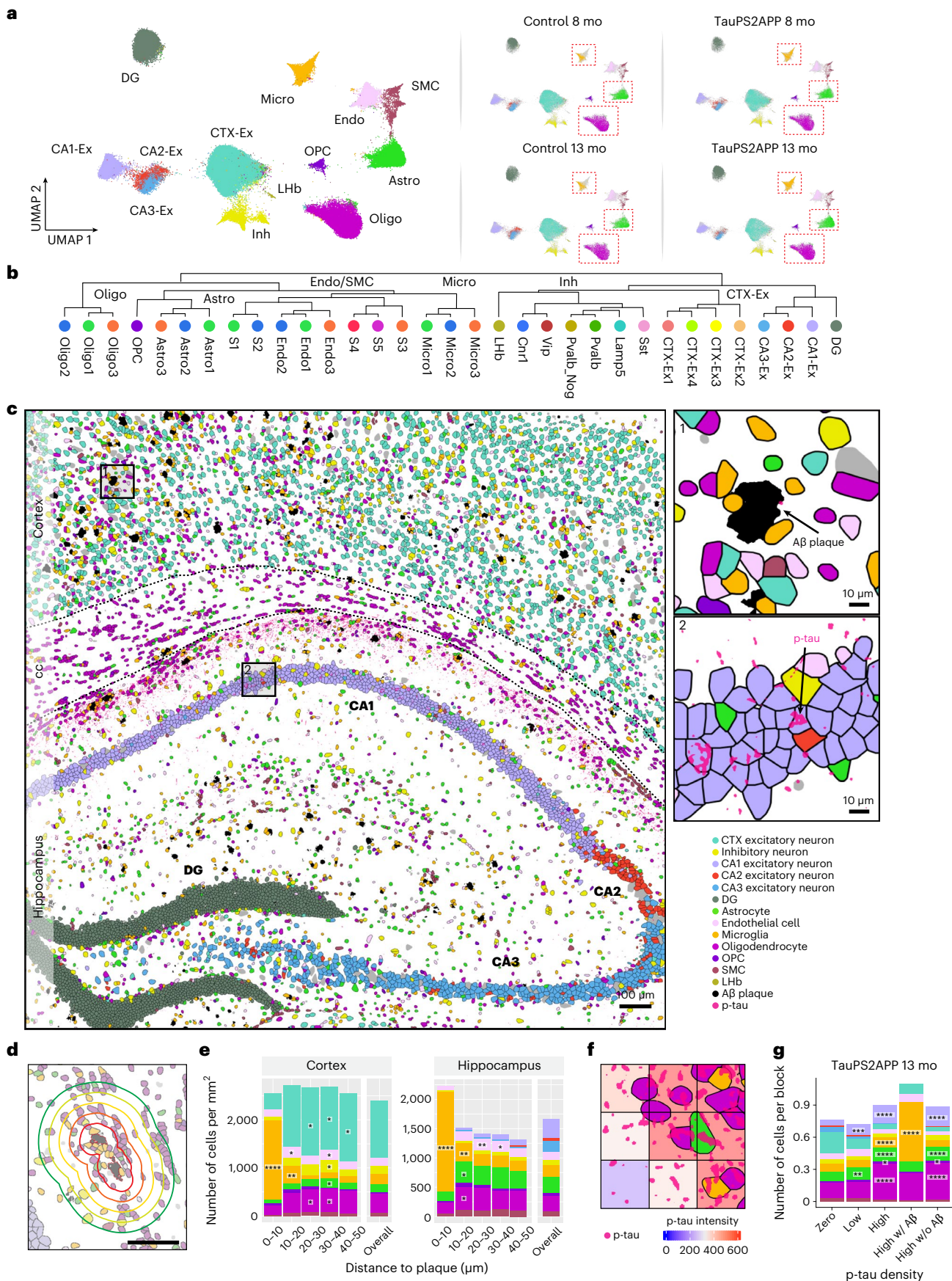
Because spatial information of RNAs was preserved at subcellular resolution, we were able to generate a high-resolution spatial cell atlas of the cortex and hippocampus in conjunction with precise localization of AD-related histopathology (Fig. 2c and Extended Data Fig. 3d). In TauPS2APP mice, the percentage of plaque area in the whole tissue rose from 0.31% (187 A β plaques identified with an average size of $129 \pm 89 \mu\text{m}^2$) in 8-month mouse brains to 0.74% (328 plaques identified with an average size of $181 \pm 141 \mu\text{m}^2$) in 13-month mouse brains. Meanwhile, no plaques were visible in nontransgenic controls (Extended Data Figs. 2a and 3d). p-tau signal was observed mostly in the hippocampal region of the TauPS2APP mice at 8 months and became more pronounced at 13 months in both hippocampal and cortical regions (Fig. 2c and Extended Data Fig. 3d).

To assess how cell distributions and cell states are affected by the nearby presence of amyloid plaque and tauopathy, we first analyzed the cell distributions and states in the cortex and hippocampus separately. Next, to quantify cell type distribution in the spatial relationship to A β plaque, we calculated the density of different cell types within the first five 10 μm intervals surrounding plaques (0–50 μm ; Fig. 2d; Methods). Among the 13 major cell types, microglia, astrocytes, oligodendrocytes, oligodendrocyte precursor cells (OPC) and endothelial cells showed relative enrichment in the vicinity of plaques in comparison with the overall density of that cell type in the cortex and hippocampus in TauPS2APP mice (Fig. 2e and Extended Data Fig. 3e,f). As expected, the most striking change was detected in microglia: they were by far the most prevalent cell type in the 10 μm ring around the plaque (Fig. 2e), where they were markedly concentrated compared with the normal density in that brain region and often seemed to be in direct contact with the plaques. Compared with their overall normal density, microglia were also more concentrated in the 10–20 μm annulus around plaques, although to a lesser degree than within 10 μm distance of plaque (Fig. 2e). The accumulation of microglia around plaque uncovered here by spatial transcriptomics is consistent with previous studies^{14,15,17}, but more detailed and unbiased, thus further validating the utility of STARmap PLUS. Astrocytes, oligodendrocytes, OPC and endothelial cells showed modest but significant enrichment at the 10–30 μm distance compared to their overall average density but were depleted in the immediate neighborhood of plaques (<10 μm). Both excitatory and inhibitory neurons were also depleted within 10 μm around A β plaques in comparison with the overall density of these neuron types (Fig. 2e and Supplementary Table 2).

p-tau (AT8) immunoreactivity was more finely dispersed in neuronal cell bodies and axon bundles. To investigate the spatial correlation of p-tau intensity with different cell types, we divided the spatial atlas into blocks of 20 μm -spaced grids (Fig. 2f) and analyzed

Fig. 2 | Top-level cell type classification and spatial analysis in the brain slices of TauPS2APP and control mice. **a**, UMAP plots showing 13 major cell types identified in the transcriptional profiles of 72,165 cells collected from eight coronal brain sections of TauPS2APP and control mice at 8 and 13 months. **b**, Hierarchical taxonomy dendrogram showing two levels annotation of the 13 top-level clusters and 33 sublevel clusters (subclusters). Cell type annotation was assigned to each cluster according to its representative gene markers compared to the rest of the cells. **c**, Representative spatial cell type atlas with A β and tau pathologies in cortical and hippocampal regions of TauPS2APP 13-month sample ($n = 2$ independent animals). The imaging area was separated into the cortex, corpus callosum (cc) and hippocampus manually with expert annotation, and the boundaries were marked by black dash lines. Zoom-in sections in the cortical region and the hippocampal region with p-tau protein signal. **d**, A schematic illustrating the spatial patterns analysis of cell type compositions around the

A β plaque. Scale bar, 50 μm . **e**, Representative spatial distribution of cell type compositions around A β plaque for TauPS2APP 13-month samples. Stacked bar plot showing the density (cell count per mm^2) of each major cell type at different distance intervals (0–10, 10–20, 20–30, 30–40 and 40–50 μm) to the A β plaque. The cell density of each major cell type in each area was included as the reference for comparison. Asterisks denote significantly enriched cell types in each distance interval. One-sided one-sample *t*-test, * $P < 0.05$, ** $P < 0.01$, **** $P < 0.0001$ versus overall cell density. **f**, Schematics illustrating the method used for p-tau signal quantification. **g**, Cell type composition analysis based on the 20 \times 20 μm grid in the TauPS2APP samples at 13 months ranked by p-tau density. Stacked bar plot showing the average number of cells per block for each major cell type. Asterisks denote significantly enriched cell types in each p-tau density bin compared to the zero p-tau bin. One-sided one-sample *t*-test, * $P < 0.05$, ** $P < 0.01$, *** $P < 0.001$, **** $P < 0.0001$ versus zero p-tau bin.



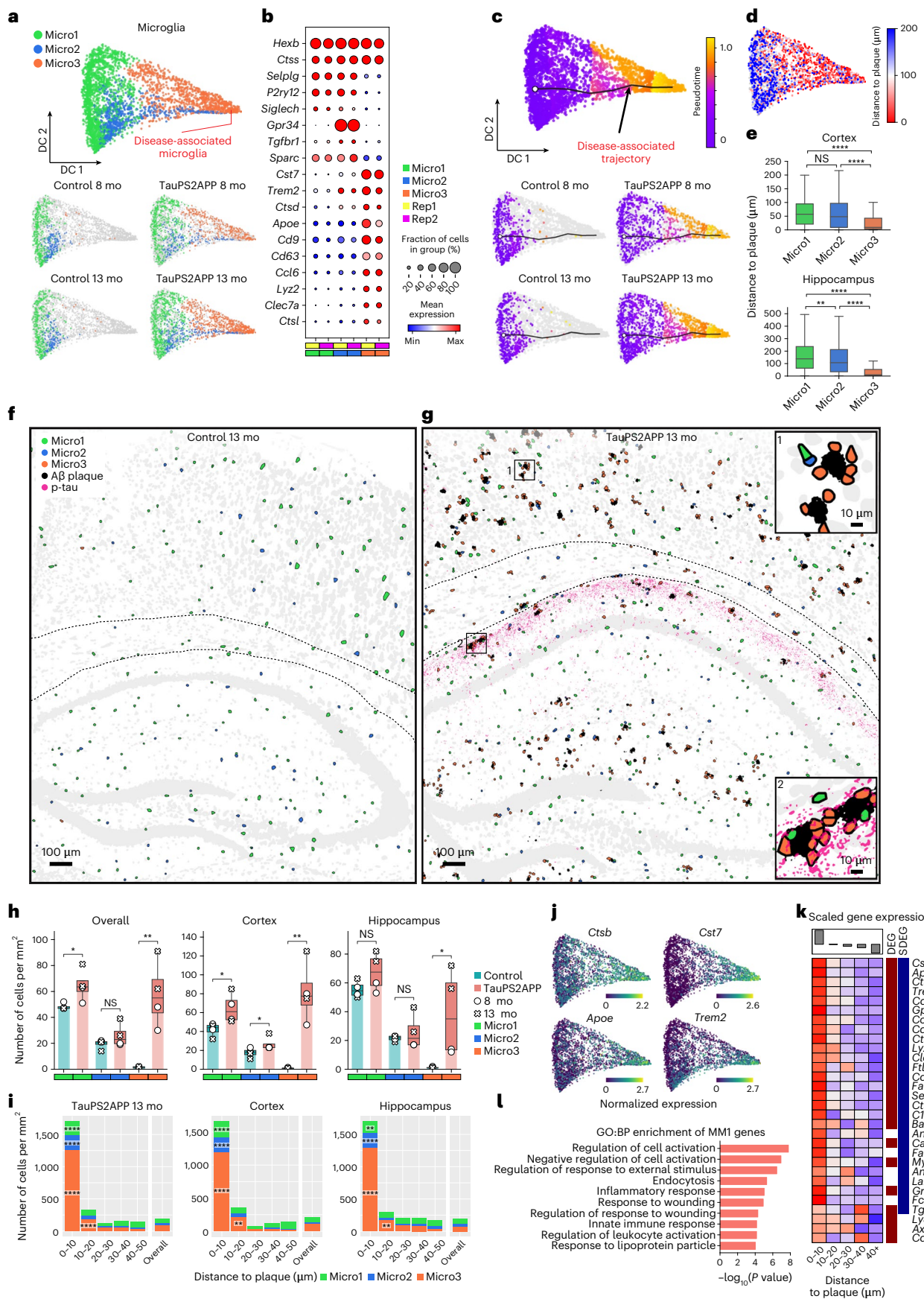


Fig. 3 | Spatiotemporal gene expression analysis of microglia in TauPS2APP and control samples. **a**, Diffusion map visualization of 3,732 microglia cells across different samples. **b**, Dot plot showing the expression level of representative gene markers among different microglia subclusters. **c**, Diffusion map with pseudotime trajectory visualization of microglia population across different samples generated by Monocle3 (ref. ⁴⁸). Colormap represents the pseudotime value and the root of the trajectory was marked by the white dot. **d**, Diffusion map plots showing the distance from each microglia cell to the closest plaque. **e**, Boxplot showing the distribution of the distance from each microglia to the closest plaque nearby among microglia subtype populations in the cortex ($n = 1,248$) and hippocampus regions ($n = 1,206$ cells). Box, 75% and 25% quantiles. Line, median. Whisker, the maxima/minima or to the median $\pm 1.5 \times$ IQR. Two-sided t -test, $**P < 0.01$, $****P < 0.0001$. **f, g**, Spatial cell maps of microglia in the 13-month control (**f**) and TauPS2APP (**g**) samples. Insets show zoom-in regions (1, 2). Dashed black lines mark the boundaries between the cortex, cc and

hippocampus. **h**, Boxplot showing the density of each microglia subcluster in all the eight sections (left), the cortex region (middle) and the hippocampus region (right) in control and TauPS2APP mice at two different time points. Box, 75% and 25% quantiles. Line, median. Dots, individual samples. One-sided t -test. $*P < 0.05$, $**P < 0.01$. **i**, Stacked bar charts showing the density of each microglia subcluster in each distance interval centered by the A β plaque at 13 months. Asterisks denote significantly enriched microglia subtypes in each distance interval. One-sided one-sample t -test, $*P < 0.05$, $**P < 0.01$, $***P < 0.0001$ versus overall cell density. **j**, Diffusion map showing the expression of four representative DEG or SDEG genes of microglia. **k**, Matrix plot showing the z scores of DEGs or SDEGs in the disease-associated gene module of microglia in each distance around the A β plaque in TauPS2APP 13-month sample. The total averaged scaled expression level in different distance intervals was visualized by the bars on top of the matrix plots. **l**, Gene ontology enrichment analysis (Fisher's one-sided test) results of disease-associated gene module in microglia.

the covariation of cell type composition versus p-tau density within these 20 μm squares. Oligodendrocytes were found most substantially enriched in the blocks with high p-tau, even where there was no amyloid plaque (Fig. 2g).

The top-level cell clustering and spatial RNA analyses revealed that microglia, astrocytes, OPCs, oligodendrocytes and neuronal cells showed the biggest changes in their transcriptional profiles, spatial distributions or both. These cell types were thus selected for in-depth subclustering analyses to pinpoint disease-associated subtypes, cell states and gene pathways in the following sections (Figs. 2b and 3–6).

DAMs directly contact A β plaques from earlier disease stage

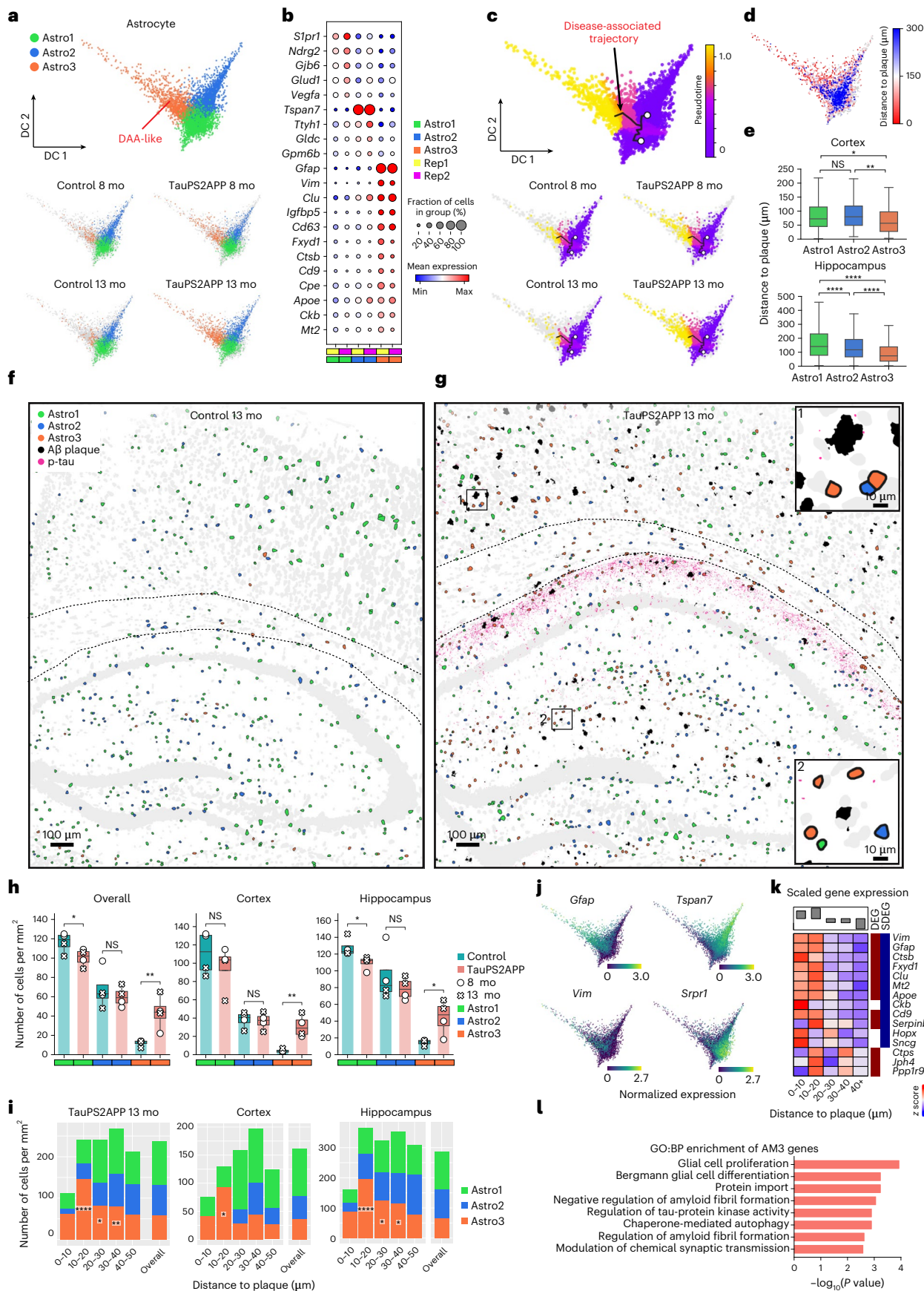
We first investigated the heterogeneity within the microglia population by subclustering analysis of transcriptomic profiles. Three subpopulations were identified and categorized as Micro1 (52%), Micro2 (21%) and Micro3 (27%) (Fig. 3a, Extended Data Fig. 4a and Supplementary Table 2). Micro1 and Micro2 subtypes were present in both TauPS2APP and control samples, while the Micro3 subpopulation cells were almost absent in controls and expanded greatly from 8 months to 13 months in the TauPS2APP brains (Fig. 3a and Extended Data Fig. 4a). Micro1 and Micro2 both express the marker *P2ry12* and may correspond to subtypes of homeostatic microglia¹⁰: Relative to Micro1, Micro2 shows upregulation of *Tgfb1* and *Gpr34*. The Micro3 subtype expressed high levels of *Cst7*, *Ctsb*, *Trem2* and *Apoe*, which are characteristic of DAM and associated with neurodegeneration¹⁰ (Fig. 3b). Furthermore, we performed single-cell transcriptomic data integration with previously published scRNA-seq studies of human AD patients¹². The Micro3 cluster had the best correspondence to the AD pathology-associated microglia subpopulation (Mic1) from human AD patient samples (Extended Data Fig. 4b,c). Given their strong association with plaques in the TauPS2APP disease model and expression of known DAM gene markers, we believe that the Micro3 population defined in STARmap PLUS is equivalent to DAM previously described in single-nucleus RNA-seq (snRNA-seq) studies^{10,16}.

It is noteworthy that clustering analysis effectively identifies distinct cell subtypes but does not capture well multistep cell state transitions. To uncover cell state transitions during disease progression and determine the relationship among different subtypes, we deployed Monocle pseudotime analysis⁴⁸, a widely used computational tool for reconstructing cell differentiation trajectory, as a complement to subtype analysis in the following sections. We aimed to reconstruct the presumptive path along which microglia alter their state by pseudotime trajectory analysis of the single-cell transcriptomic profiles (Fig. 3c). By this computational approach, the microglia population showed a linear pseudotime trajectory that aligned well with the actual disease progression timeline: microglia in control mice were enriched at the starting point of the trajectory while those in TauPS2APP mice shifted along the trajectory from 8 to 13 months (left-to-right; Fig. 3c). We then measured the distance from each microglia to the closest plaque in the same tissue section and visualized that on the diffusion map along with our pseudotime calculation (Fig. 3d). The correlation of distance from plaque with pseudotime trajectory suggests that one of the driving forces of the trajectory could be plaque-induced genes in space, which agrees with the fact that DAM microglia lie in closest proximity to plaque (Fig. 3d,e).

We then performed detailed spatial analyses of microglia subtypes Micro1–3. In the cortex, all three microglial subtypes showed significant increases in overall density at both ages of TauPS2APP mice; in the hippocampus, the increased density of microglia was statistically significant only for Micro3 (Fig. 3f–i and Extended Data Fig. 4d). With the cell type composition analysis around A β plaques, we found that (1) Micro3 is the most predominant cell type (>70%) within the 10 μm ring around plaque in cortex and hippocampus at both 8 and 13 months age (Fig. 3i and Extended Data Fig. 4e); (2) Micro1 and Micro2 cells were also enriched within 10 μm distance around the plaques in both the cortex and hippocampus (Fig. 3i, Extended Data Fig. 4e and Supplementary Table 2); (3) from 8 months to 13 months, the density of

Fig. 4 | Spatiotemporal gene expression analysis of astrocytes in TauPS2APP and control samples. **a**, Diffusion map visualization of 6,789 astrocytes across samples. **b**, Dot plot showing the expression level of representative markers across different astrocyte subclusters. **c**, Diffusion map with pseudotime trajectory visualization of the astrocyte cell population across different samples generated by Monocle3. Colormap represents the pseudotime value and the root of the trajectory was marked by the white dot. **d**, Diffusion map showing the distance from each microglia cell to the closest plaque. **e**, Boxplot showing the distribution of the distance from each astrocyte to the closest plaque among astrocyte subtype populations in two different brain regions ($n = 1,215$ and 2,057 cells). Top: cortex; bottom, hippocampus. Box, 75% and 25% quantiles. Line, median. Whisker, the maxima/minima or to the median $\pm 1.5 \times$ IQR. Two-sided t -test, $*P < 0.05$, $**P < 0.01$, $***P < 0.0001$. **f, g**, Spatial cell maps of astrocyte population in 13-month control (**f**) and TauPS2APP (**g**) samples. Insets show the zoom-in (1, 2). Dashed black lines mark the boundaries between the cortex,

cc and hippocampus. **h**, Boxplot showing the density of each astrocyte subcluster in all eight sections (left), the cortex (middle) and hippocampus region (right) in control and TauPS2APP mice at two different time points. Box, 75% and 25% quantiles. Line, median. Dots, individual samples. One-sided t -test, $*P < 0.05$, $**P < 0.01$. **i**, Stacked bar charts showing the density of astrocyte subcluster in each distance interval around the A β plaque at 13 months. Asterisks denote significantly enriched astrocyte subtypes in each distance interval. One-sided one-sample t -test, $*P < 0.05$, $**P < 0.01$ versus overall cell density. **j**, Diffusion map showing the expression of four representative top DEGs of astrocyte. **k**, Matrix plot showing the z scores of DEGs or SDEGs in the disease-associated gene module of astrocyte in each distance interval around the A β plaque in TauPS2APP 13-month sample. The total averaged scaled expression level in different distance intervals was visualized by the bars on top of the matrix plots. **l**, Gene ontology enrichment analysis (Fisher's one-sided test) results of disease-associated gene module in astrocyte.



Micro3 increased within the 10 µm ring near plaque, whereas the local cell density of Micro1 and Micro2 near plaque (<10 µm) remained the same or fell (Fig. 3*i*, Extended Data Fig. 4*e* and Supplementary Table 2) and (4) Micro3 density increased also in the 10–20 µm annulus around plaque (Fig. 3*i* and Extended Data Fig. 4*e*). Together, the spatial analysis of microglia cell subtypes suggest that microglia activation strongly correlates with their close association with plaques (<20 µm), and the elevated concentration of all three subtypes around plaques suggests a local transition from Micro1 and Micro2 to Micro3 near plaque during disease progression.

To get a better understanding of microglia response to plaques and tau pathology at the molecular level, we analyzed differentially expressed genes (DEGs) of microglia along disease progression and in relation to plaques (Extended Data Fig. 4*f* and Supplementary Table 3). Most of the upregulated microglial DEGs identified in TauPS2APP mouse brains overlap with Micro3 (DAM) gene markers and coincide with genes that are upregulated near plaques in this study, which we identified as ‘spatial DEG’ (SDEG) (Fig. 3*j*, Extended Data Fig. 4*g* and Supplementary Table 4); these genes are involved in biological processes such as regulation of cell death (that is, *Ccl3*, *C1qa* and *Ctsd*) and regulation of cell migration (that is, *Cd9*, *Apoe* and *Trem2*) (Extended Data Fig. 4*f,h*). We also performed gene module analysis using single-cell weighted gene co-expression network analysis (scWGCNA)⁴⁹. Seven gene modules were identified in microglia, and among them, microglia module 1 (MM1) showed the most significant DEG enrichment and upregulated gene expression in plaque-proximal regions (Extended Data Fig. 4*i,j* and Supplementary Table 5). Based on these features, we identified MM1 as the disease-associated module in microglia. Indeed, MM1 contained many DAM marker genes, such as *Cst7*, *Trem2* and *Cd63*, and these genes were also identified as DEGs or SDEGs (Fig. 3*k*). The GO analysis showed that the MM1 module genes were involved in cell activation (that is, *Cst7*, *Cd83* and *Trem2*) and inflammatory response (that is, *C1qa*, *Apoe* and *Grn*) (Fig. 3*l*).

DAAs emerge near the plaque-DAM complex at a later stage

Astrocyte was another non-neuronal cell type that showed significant changes in TauPS2APP versus control. Subclustering analysis of the astrocytes identified three transcriptionally distinct subpopulations Astro1(54%), Astro2(32%) and Astro3(14%) (Fig. 4*a*, Extended Data Fig. 5*a* and Supplementary Table 2). Astro3 cells were occasionally found in control mice, but the Astro3 subpopulation expanded in TauPS2APP mice, increasing from 8 to 13 months (Fig. 4*a* and Extended Data Fig. 5*a*). Transcriptomic changes in Astro3 astrocytes resembled those of DAA previously described in AD models, characterized by upregulation of genes such as *Gfap*, *Vim* and *Ctsb* (Fig. 4*b*)⁹. To test whether this Astro3 cell population exists in other AD datasets, we performed single-cell transcriptomic data integration with previously published single-cell RNA-seq studies of human AD patients and 5xFAD mouse model^{9,12} (Extended Data Fig. 5*b–h*; Methods). The Astro3 cluster identified from

STARmap PLUS spatial transcriptomic data had the best correspondence to AD pathology-associated astrocyte subpopulation (Ast1) from human AD patient samples¹² and to disease-associated astrocytes (DAA; cluster 4) in the 5xFAD mouse model⁹ (Extended Data Fig. 5*e–h*). Based on this transcriptomic similarity and their association with TauPS2APP mice, we annotated the Astro3 subtype as ‘DAA-like’ cell population.

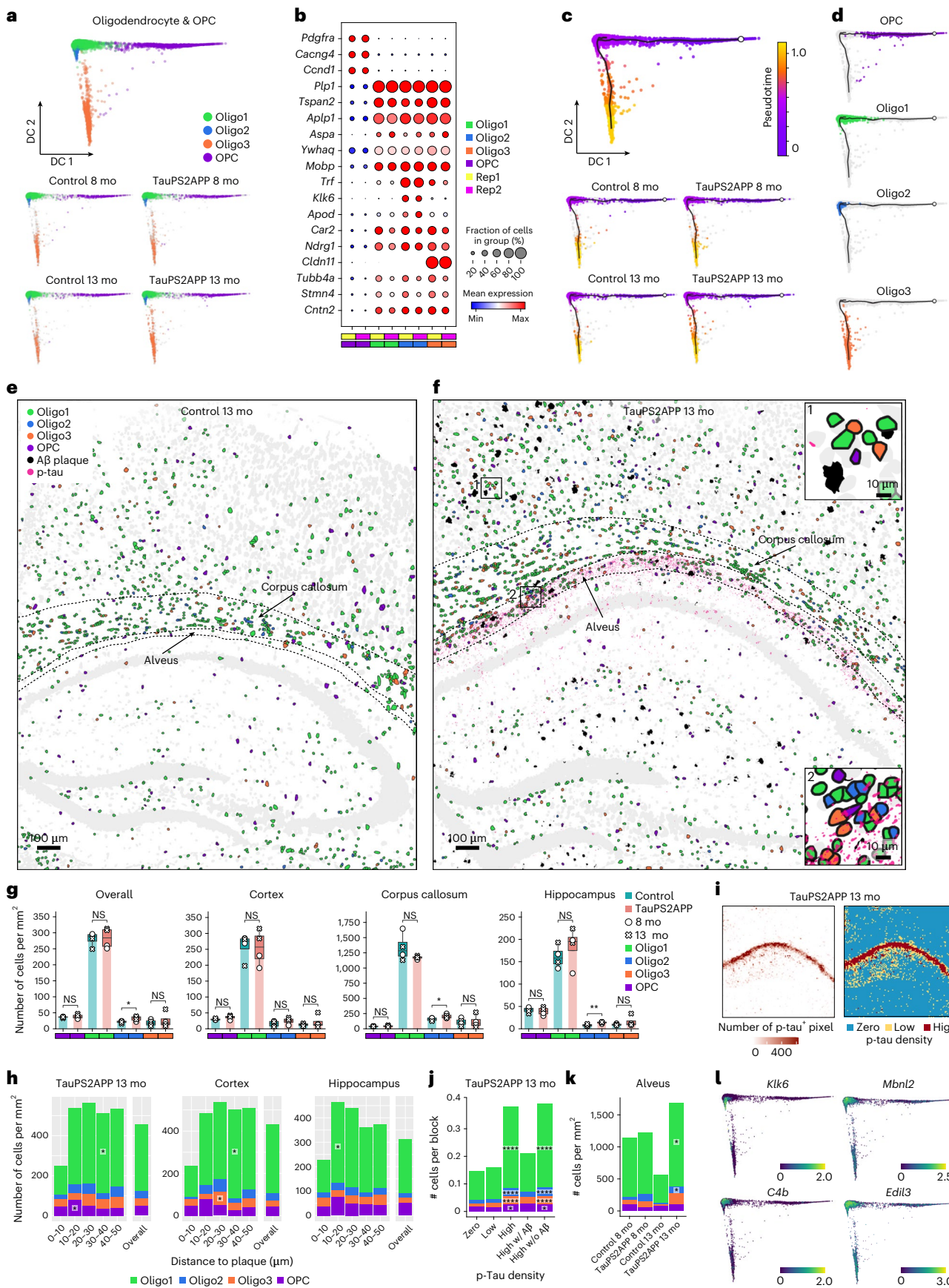
The pseudotime trajectory analysis of astrocytes yielded a 3-branched trajectory, with one side connecting Astro1 and Astro2, which represent two subtypes of ‘homeostatic’ astrocytes that differ by gene expression, and a longer branch that is associated with disease. Therefore, the trajectories were annotated with two starting points from Astro1 and Astro2, and one endpoint to Astro3 (DAA-like) (Fig. 4*c*). Similar to microglia, we further validated our annotation by visualizing the distance from each cell to its nearest plaque on the diffusion map embedding; this analysis showed gradients consistent with the pseudotime values (Fig. 4*d*). Statistical analysis further confirmed that the Astro3 population on average was located closer to plaque than either Astro1 or Astro2 homeostasis populations (Fig. 4*e*).

The spatial cell map of astrocyte subtypes showed that Astro1 cells are preferentially located near the cell bodies of cortical and hippocampal neurons, whereas Astro2 cells are more abundant in corpus callosum, hippocampal neuropil layer and stratum lacunosum-moleculare (Fig. 4*f–h* and Extended Data Fig. 6*a*). Cell type analysis in relation to tissue pathology revealed that while DAM microglia closely surround plaque (mostly <10 µm), Astro3 (DAA-like) cells were substantially enriched around plaque at an intermediate distance (10–40 µm) in TauPS2APP mice at both 8 months and 13 months, and in both cortex and hippocampus (Fig. 4*i*, Extended Data Fig. 6*b* and Supplementary Table 2). At 8 months but not 13 months, Astro2 was also enriched near the plaques (10–30 µm) as the major astrocyte subtype in the hippocampus (Extended Data Fig. 6*b* and Supplementary Table 2). The observed shift of the astrocyte population around plaque from Astro2 to Astro3 from 8 to 13 months suggests that there might be a conversion of Astro2 to Astro3 near plaques during disease progression in the hippocampus.

The DEGs from the astrocytes of TauPS2APP versus control samples were related to GO terms glial cell differentiation and gliogenesis (that is, *Vim*, *Clu* and *Gfap*) (Extended Data Fig. 6*c,d* and Supplementary Table 3). The gene expression profiles of top DEGs plotted on the pseudotime embedding showed that the expression pattern of *Gfap* and *Vim* correlated with the DAA-like population, whereas *Spr1* and *Tspan7* correlated with the two homeostasis populations Astro1 and Astro2, respectively (Fig. 4*j*). Cell-type-resolved SDEG analysis around plaques in the 13-month TauPS2APP mice further supports the spatial enrichment of DAA-like cells and their gene markers near plaques, especially obvious in the 10–20 µm ring around plaques (Extended Data Fig. 6*e* and Supplementary Table 4). The scWGCNA identified four gene modules in astrocytes, of which module 3 (AM3) showed the most significant DEG enrichment and upregulation in near-plaque regions

Fig. 5 | Spatiotemporal gene expression analysis of oligodendrocyte lineage cells in TauPS2APP and control samples. **a**, Diffusion map visualization of 11,265 oligodendrocytes and 1,269 OPCs across samples. **b**, Dot plot showing the expression level of representative markers across different oligodendrocyte subclusters and OPC. **c**, Diffusion map with pseudotime trajectory visualization of oligodendrocyte and OPC population across different samples generated by Monocle3. Colormap represents the pseudotime value. The trajectory starting anchor was marked by the white dot and manually selected based on the OPC population. **d**, Diffusion map plots showing different types of oligodendrocytes identified in **a** along with trajectory identified in **c**. **e,f**, Spatial cell map of oligodendrocyte and OPC population in 13-month control (**e**) and TauPS2APP (**f**) samples. Insets show the zoom-in regions (1, 2). Dashed black lines mark the boundaries between the cortex, cc, hippocampus and alveus. **g**, Boxplot showing the density of each oligodendrocyte subcluster and OPC in all eight sections (left) and other separated brain regions (right) in control and TauPS2APP mice at two different time points. Box, 75% and 25% quantiles. Line, median. Dots, individual

samples. One-sided *t*-test, **P*<0.05, ***P*<0.01. **h**, Stacked bar charts showing the density of each oligodendrocyte subcluster and OPC in each distance interval around the Aβ plaque at 13 months. Asterisks denote significantly enriched oligodendrocyte subtypes and OPC in each distance interval. One-sided one-sample *t*-test, **P*<0.05 versus overall cell density. **i**, Heatmap showing p-tau quantification (left) and rank (right) of each grid in TauPS2APP sample at 13 months. **j**, Cell type composition analysis of oligodendrocyte lineages in relation to p-tau pathology. Asterisks denote significantly enriched oligodendrocyte subtypes and OPC in each p-tau density bin compared to the zero p-tau bin. One-sample *t*-test, **P*<0.05, *****P*<0.0001 versus zero p-tau bin. **k**, Cell density and subtype composition of oligodendrocyte and OPC in the hippocampal alveus region. Asterisks denote significantly enriched oligodendrocyte subtypes in the region of TauPS2APP samples compared to the paired control samples. Student’s *t*-test, one-sided **P*<0.05. **l**, Diffusion map showing the expression of four representative DEG or SDEG genes of oligodendrocytes.



(Extended Data Fig. 6f,g and Supplementary Table 5); therefore, we identified AM3 as the disease-associated gene module in astrocyte. AM3 contains many DAA marker genes, such as *Gfap*, *Vim* and *Clu*, and these genes were also identified as DEG or SDEG in astrocytes (Fig. 4k). The GO analysis suggested that the AM3 module genes are involved in glial cell proliferation, regulation of amyloid fibril formation and regulation of tau-protein kinase activity, which suggests the disease relevance of this gene module (Fig. 4l).

Oligodendrocyte lineage in the vicinity of plaques and p-tau

Subclustering analysis identified four subtypes within the oligodendrocyte lineage (Fig. 5a,b, Extended Data Fig. 7a and Supplementary Table 2): Oligo1 (77%), Oligo2 (7%), Oligo3 (6%) and OPC (10%). The oligodendrocyte gene marker *Plp1* marks all three oligodendrocyte subtypes (Oligo1-3), whereas differential expression of other genes such as *Klk6* and *Cldn11* marks Oligo2 and Oligo3 populations, respectively (Fig. 5b). The pseudotime trajectory analysis of the combined population of OPC and oligodendrocyte cells recapitulated the known differentiation path from OPC to mature oligodendrocytes (Fig. 5c,d). The expression pattern of the oligodendrocyte lineage marker genes among the Oligo subclusters further supports the biological relevance of the pseudotime trajectory (Extended Data Fig. 7b).

All four oligodendrocyte subtypes were present in TauPS2APP and control brains (Fig. 5e-g and Extended Data Fig. 7c). Only the Oligo2 population showed significantly elevated abundance in TauPS2APP mice, especially in the corpus callosum and hippocampus, in association with tau and amyloid pathology (Fig. 5e-g). Around amyloid plaques in TauPS2APP mice, OPCs were enriched in the 10–20 µm ring at both 8 and 13 months, accumulating to a 64–84% higher density than its overall density (Fig. 5e-h, Extended Data Fig. 7c,d and Supplementary Table 2). Among all oligodendrocytes, Oligo1 is the predominant (>70%) subtype around plaques and showed a statistically significant enrichment around amyloid plaques at both 8 and 13 months (Fig. 5h, Extended Data Fig. 7d and Supplementary Table 2). At 13 months, Oligo3 increased by 25–60% within the 20–40 µm distance from the plaques and was statistically significant in the 20–30 µm distance in the cortex of TauPS2APP mice in comparison with the overall density (Fig. 5h).

Given that the density of oligodendrocytes is positively correlated with the density of p-tau, independently of amyloid (Fig. Fig. 2), we sought to pinpoint which oligodendrocyte subtype is spatially associated with tauopathy. Using the aforementioned grid-based spatial correlation analysis, we found that in the 13-month TauPS2APP mice, the cell density of all three oligodendrocyte subtypes and OPC substantially increased in regions with higher p-tau signals in the absence of Aβ pathology (Fig. 5i,j). We observed that p-tau signals were concentrated in the alveus of the hippocampus, which contains axon bundles of hippocampal neurons (alveus, Fig. 5i,k). Compared with 13-month control mice, the oligodendrocyte densities increased markedly (two- to four-fold) in the alveus region of 13-month TauPS2APP mice (Fig. 5k). In total, the spatial analysis of cells of the oligodendrocyte lineage in

relation to p-tau revealed a strong association between tauopathy and the accumulation of oligodendrocytes subtypes (Fig. 5j,k).

Through analyzing the DEGs in oligodendrocytes, we identified and verified a group of genes (such as *Klk6* and *Cd9*) that were strongly upregulated in 13-month-old TauPS2APP mice compared to the same age control mice (Extended Data Fig. 7f and Supplementary Table 3). The DEG analysis also showed that the astrocyte marker gene *Gfap* was upregulated in both microglia and oligodendrocytes of 13-month-old TauPS2APP mice (Extended Data Figs. 4f and 7f). While *Gfap* mRNA has been detected in nonastrocytes by snRNA-seq^{8,12}, we cannot exclude that the observed expression of *Gfap* by oligodendrocytes in our spatial transcriptomics data is due to its presence in the processes of astrocytes that physically surround other cell types. GO term analysis indicated the involvement of oligodendrocyte DEGs in glial cell development (that is, *Mobp* and *Plp1*) and myelination (that is, *Mbp* and *Tspan2*) during disease progression (Extended Data Fig. 7f,g). Interestingly, SDEG analysis of oligodendrocytes near plaques revealed increased expression of these genes, suggesting subpopulation(s) of oligodendrocytes (with elevated expression of *C4b* and *Klk6*) might be responding to plaques or interacting with other cells or cellular compartments (microglia, astrocytes and/or dystrophic neurites) that are affected by amyloid pathology (Fig. 5l, Extended Data Fig. 7h and Supplementary Table 4). The scWGCNA identified four gene modules in oligodendrocytes, of which module one (OM1) showed the most significant DEG enrichment and was also upregulated in near-plaque regions (Extended Data Fig. 7i-k and Supplementary Table 5), suggesting that OM1 was the disease-associated gene module in oligodendrocytes. GO analysis showed that the OM1 module genes are involved in myelination and axon ensheathment (Extended Data Fig. 7l).

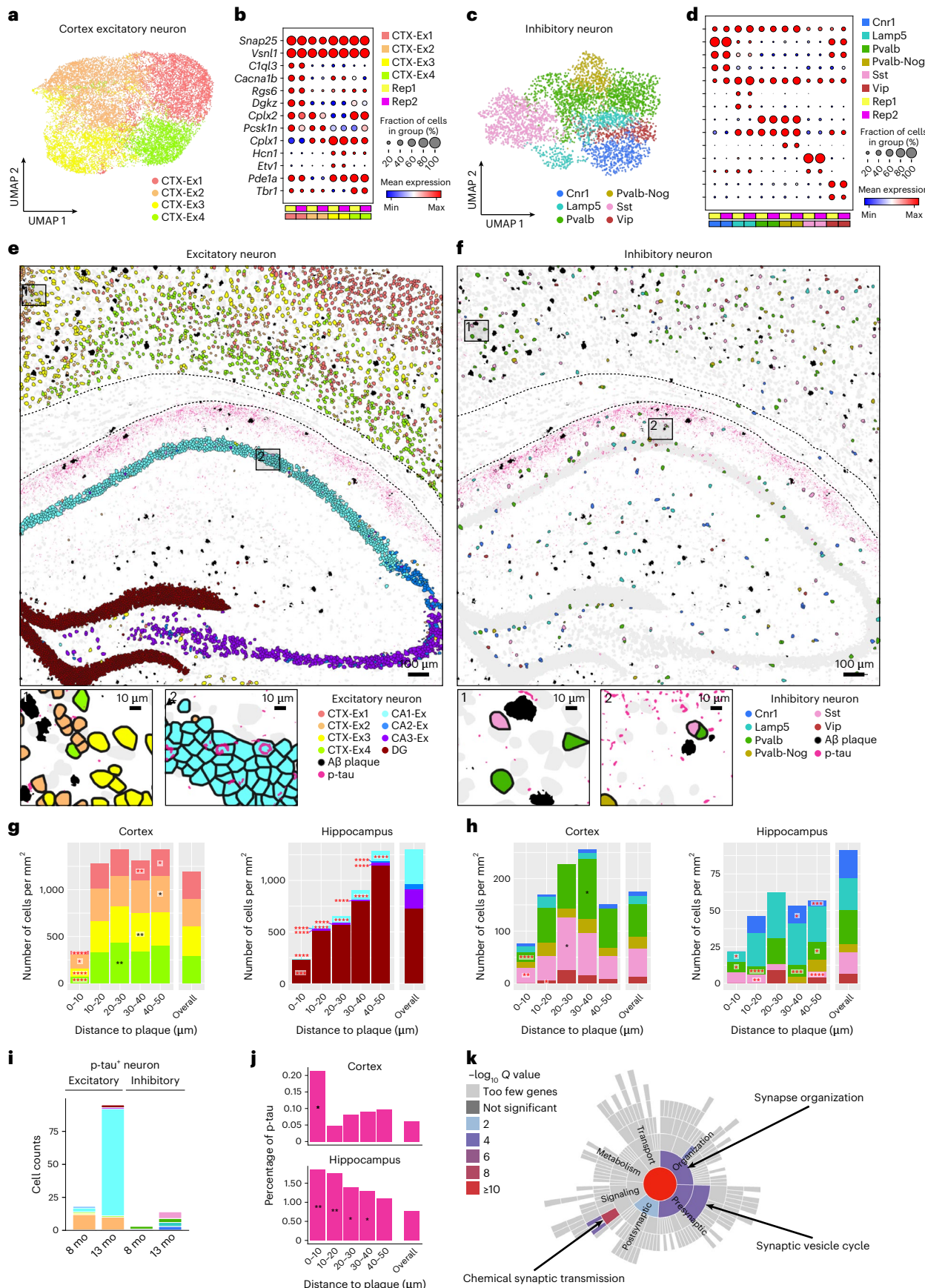
Susceptibility of neuron to Aβ plaques and p-tau

Besides cellular changes in glial cells, the transcriptomic responses in neurons are critical for understanding the mechanisms of neurodegeneration. Subclustering transcriptomic analysis of the neurons in the cortex and hippocampus identified eight excitatory neuron subtypes and six inhibitory neuron subtypes (Fig. 6a-d). As visualized in the spatial cell map of neurons (Fig. 6e,f and Extended Data Fig. 8), the four subtypes of cortical excitatory neurons correspond to different cortical layers (CTX-Ex1 corresponds to layers 2/3, CTX-Ex2/3 corresponds to layers 4/5, CTX-Ex4 corresponds to layer 6); the excitatory neuronal types in the hippocampal region correspond to the principal cells of DG, CA1, CA2 and CA3. Among the four subtypes of inhibitory neurons, Pvalb and Sst neurons were present at higher density in the cortex while Cnr1 and Lamp5 neurons were more abundant in the hippocampus (Extended Data Fig. 9a,b).

We investigated neuron subtype compositions and their transcriptomic profiles in relation to Aβ plaques. In the cortex, there was a notable paucity (strong relative reduction) of all types of neurons adjacent to plaques (<10 µm; Fig. 6g,h and Extended Data Fig. 9c,d), anticorrelating with the large increase in density of microglia close to plaque. In the hippocampus, the impact of plaque on the density of

Fig. 6 | Spatiotemporal gene expression analysis of neurons in TauPS2APP and control samples. **a**, UMAP visualization showing four subclusters of cortex excitatory neuron ($n = 18,303$). **b**, The expression level of representative gene markers among different subclusters of cortex excitatory neuron cells. **c**, UMAP visualization showing six subclusters of inhibitory cell ($n = 4,163$). **d**, The expression level of representative gene markers among different subclusters of inhibitory neuron cells. **e,f**, Top: Spatial map of Aβ plaque and p-tau with excitatory (e) and inhibitory (f) neurons in the TauPS2APP 13-month samples. Bottom: high magnification views of areas indicated in the black boxes on the top panel. **g,h**, Stacked bar charts showing the density of each subcluster of excitatory (g) and inhibitory (h) neuron population from different brain regions at different distance intervals to the Aβ plaque of the 13-month TauPS2APP sample. Black asterisks denote significantly enriched neuron subclusters in each distance interval. Red asterisks denote significantly decreased neuron

subclusters in each distance interval. One-sided one-sample *t*-test, * $P < 0.05$, ** $P < 0.01$, *** $P < 0.001$, **** $P < 0.0001$ versus overall cell density. **i**, Stacked bar charts showing the composition of p-tau⁺ excitatory neurons and inhibitory neurons in TauPS2APP mice at two different time points defined by the ratio of tau⁺ pixels to the area of each cell (Methods). **j**, p-tau signal quantification around plaques. p-tau⁺ pixels (intensity > threshold; Methods) were quantified at a different distance to the Aβ plaque in the cortex and subcortical regions of the TauPS2APP 13-month samples. Asterisks denote regions with statistically significantly higher p-tau percentage compared to the overall p-tau percentage. One-sided one-sample *t*-test, * $P < 0.05$, ** $P < 0.01$ versus overall p-tau percentage. **k**, Synaptic gene ontology (SynGO) term enrichment of DEGs ($P < 0.05$) identified from the p-tau⁺ CA1 neurons versus p-tau⁻ CA1 neurons in the 13-month TauPS2APP samples using SynGO. Color of the sunburst plot represents $-\log_{10} Q$ value at 1% FDR.



neuron subtypes was difficult to interpret because of the anatomic organization of the hippocampus and because amyloid plaques were concentrated in the neuropil, relatively far from the cell body layers and mostly in the molecular layer of dentate gyrus (Fig. 6g and Extended Data Fig. 9c).

To investigate the neuronal transcriptomic alterations induced by tauopathy, we first identified p-tau positive ($p\text{-tau}^+$) neurons whose cell bodies contained positive voxels of p-tau immunostaining signals (Methods). There was zero detectable $p\text{-tau}^+$ neuron in control mice. In TauPS2APP mice, there were five times more $p\text{-tau}^+$ neurons at 13 months than at 8 months. At 8 months, the majority of $p\text{-tau}^+$ neurons were CTX-Ex2 excitatory neurons, whereas at 13 months the majority of $p\text{-tau}^+$ neurons were the CA1 excitatory neurons of hippocampus. Inhibitory neurons account for <20% of $p\text{-tau}^+$ neurons, most of them were Pvalb neurons at 8 months, whereas at 13 months, most of them came from the Sst population (Fig. 6i). We also quantified the p-tau signal around the plaques and found that the p-tau signal was enriched within 10 μm distance near plaques (Fig. 6j). Considering neuronal cell bodies were relatively depleted within the 10 μm range, the observed p-tau signals are likely to be included in the dystrophic (injured) neurites that accumulate around plaques⁴⁰.

We finally examined the DEGs of all neuronal types in response to A β plaques and p-tau. SynGO analysis⁴² of DEGs in $p\text{-tau}^+$ CA1 neurons at 13 months revealed changes in synapse organization, synaptic vesicle cycle and chemical synaptic transmission (Fig. 6k). DEGs in all neurons of TauPS2APP at 13 months were enriched in synapse assembly, regulation of presynaptic membrane potential and chemical synaptic transmission (Extended Data Fig. 9e). Given the previously reported associations between dentate gyrus neurons and AD⁵⁰, we also examined the DEGs of the dentate gyrus neurons, which are related to synaptic transmission as well as nervous system development and regulation of synaptic plasticity (Extended Data Fig. 9f,g).

Integrative analysis of disease-associated cells and genes

The analyses above focused on dissecting disease-associated subtypes and DEGs within major brain cell types. To synthesize a comprehensive picture of AD gene pathways from multiple cell types, we performed integrative analyses of disease-associated cells and genes. We identified plaque-associated SDEGs from all cell types by clustering genes based on their expression profiles as a function of distance from amyloid plaques (Fig. 7a). We identified six clusters of SDEGs as follows: clusters 1–3 are specifically upregulated at different distances near plaques and can be regarded as PIGs (listed in Fig. 7b–d) and cluster 4–6 are relatively downregulated near plaques and enriched with neuronal genes (Supplementary Table 4). We identified 49 PIGs at 8 months and 76 PIGs in the TauPS2APP sample at 13 months with adjusted $P < 0.05$ (Fig. 7e). Thirty-six of 49 PIGs in the 8-month TauPS2APP sample were also found in the 13-month samples (Fig. 7e). The PIGs enriched within 10 μm distance from plaques were mainly DAM marker genes, such as *Trem2*, *Cst7*, *Ctsb*, *Apoe* and *Cd9* (Fig. 7b,c). The Astro3 marker *Vim* was upregulated in the regions 10–20 μm away from plaques in AD13-month

samples (Fig. 7c), which is consistent with our previous finding that DAA-like cells enriched in the 10–20 μm ring (Fig. 4). Although SDEGs in cluster 4–6 (Supplementary Table 4) are less substantially upregulated at the near plaque regions and not defined as PIGs, they are also valuable to reveal potential disease mechanisms. Comparing our PIGs with previously reported PIGs identified from 18-month AppNL-G-F mice³⁸, 19 of 49 and 21 of 76 PIGs in our TauPS2APP 8-month and 13-month samples, respectively, overlapped with previously reported PIGs (Fig. 7e). A major advantage of STARmap PLUS is that its single-cell resolution enables the identification of cell type resolved SDEGs (Extended Data Figs. 4g, 6e and 7h). We performed a comparative GO analysis^{51,52} using cell type resolved SDEGs from three major glial cell types (microglia, astrocytes and oligodendrocytes; Fig. 7f), showing cell type dependent enrichment patterns in the biological processes of neuroinflammatory response, apoptotic neuron death, glial cell differentiation, synaptic transmission, vesicle fusion and secretion hormone levels.

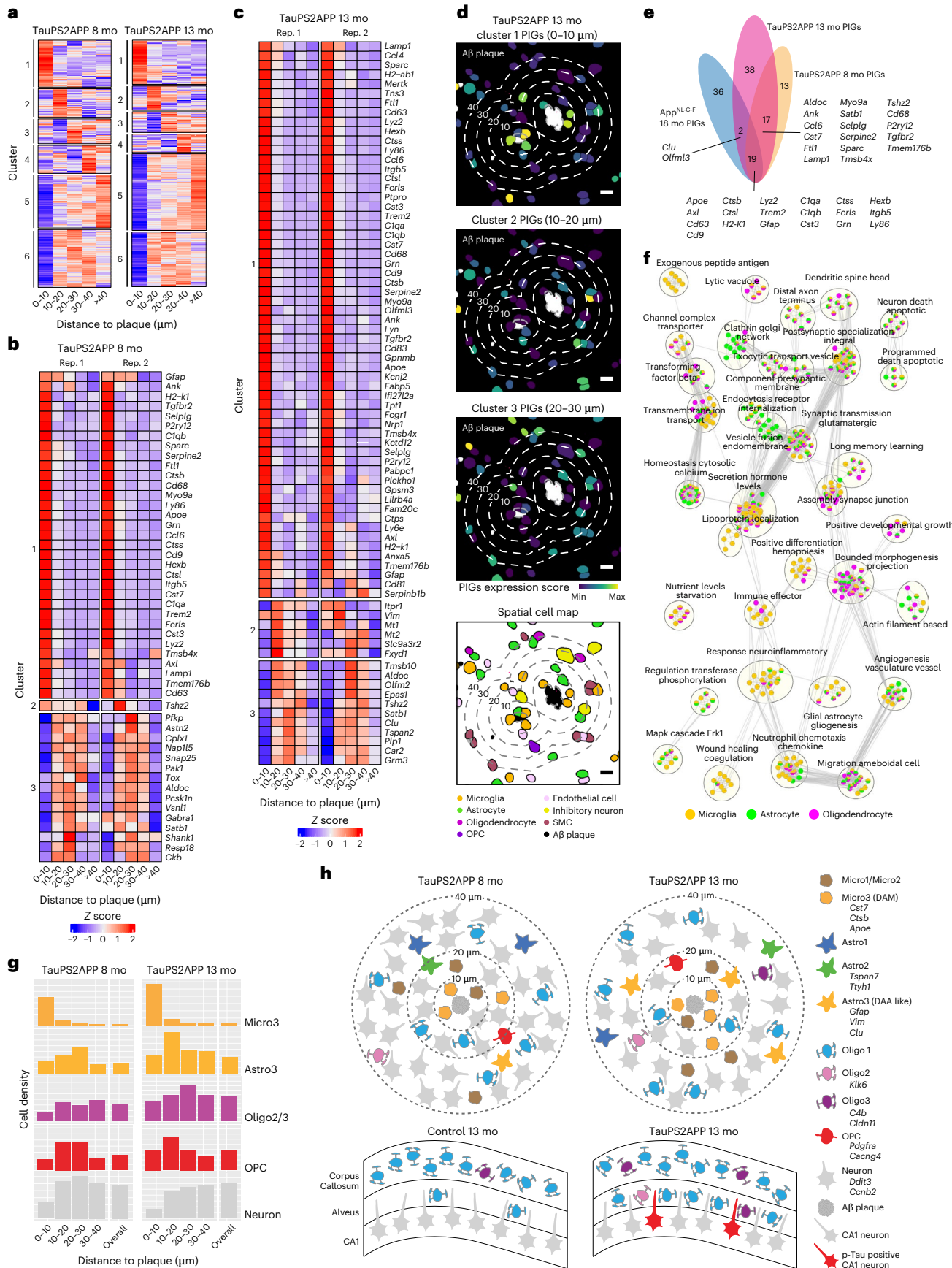
To validate the findings from the study, we repeated the STARmap PLUS experiment on a separate set of TauPS2APP mice, this time using a focused subset of genes (64 key cell type marker genes and disease-associated genes; Supplementary Tables 1,2 and Extended Data Fig. 10). We first validated STARmap PLUS by including an additional protein staining of anti-GFAP antibody, which showed consistent co-expression pattern between GFAP mRNA and protein signals and confirmed the accuracy of cell type identifications in STARmap PLUS procedures (Extended Data Fig. 10e–h). The focused 64 gene analysis yielded cell clustering results, DEG data and spatial map information that were highly consistent with the major conclusions derived from the 2,766 gene datasets including the spatial enrichment of various glial cells surrounding plaques (Extended Data Fig. 10i), the infiltration of oligodendrocytes in hippocampus alveus (Extended Data Fig. 10j) and cell type resolved DEGs and SDEGs (Extended Data Fig. 10k–m).

Discussion

Here we developed STARmap PLUS for *in situ* detection of RNAs and proteins in the same tissue section at subcellular resolution. Compared to previously reported image-based *in situ* transcriptomics methods (that is, original STARmap, MERFISH, ISS and BOLORAMIS)^{30,34,35,37}, we have substantially improved the number of *in situ* sequenced genes in tissues and enabled simultaneous profiling of RNAs and proteins in intact hydrogel-tissue scaffolds. Spatial barcoding followed by next-generation sequencing methods (such as spatial transcriptomics and slide-seq)^{31,32} enables whole transcriptome detection; however, these methods lack single-cell or subcellular resolution and cannot detect RNA and protein simultaneously in the same tissue section. The development of STARmap PLUS enables a multimodal analysis of spatially distributed RNAs and proteins, affording an opportunity to study biological systems in a more comprehensive manner. This method is widely applicable to studies of physiological and pathological mechanisms in diverse healthy and diseased tissues by integrative mapping of single-cell transcriptomic states, tissue morphology and disease markers.

Fig. 7 | Integrative spatiotemporal analysis of disease-associated cell types and gene programs. **a**, Matrix plot showing the gene clustering results in each distance interval around the A β plaque in TauPS2APP 8-month samples (left) and TauPS2APP 13-month samples (right). Colored by row-wise z score. **b,c**, Matrix plot showing the PIGs (enriched in 0–30 μm interval, adjusted $P < 0.05$) in each distance interval around the A β plaque in TauPS2APP 8-month sample (**b**) and TauPS2APP 13-month sample (**c**). Colored by row-wise z score. **d**, Representative images showing the spatial pattern of the gene set score for three spatial DEG clusters and corresponding cell type composition around plaque in the TauPS2APP mice at 13 months. Five concentric boundaries that are 10, 20, 30, 40 and 50 μm from each plaque were generated to quantify the cell type composition of each layer. Scale bar, 10 μm . **e**, Venn diagram highlighting the overlap of SDEGs in the TauPS2APP 8- and 13-month samples with SDEGs in TauPS2APP and previously reported PIGs in 18-month AppNL-G-F mice.

f, An enrichment map showing the substantially enriched GO terms of cell type resolved SDEGs of microglia, astrocyte and oligodendrocyte in the TauPS2APP 13-month samples. Nodes represent the enriched GO terms; the size of each node corresponds to the number of genes in the GO terms (gProfiler term threshold: Fisher's one-tailed test, $P < 0.05$; cytoscape node cut-off: FDR $q < 0.1$). Edges between nodes represent overlapping genes between two GO terms. Clusters with less than five nodes are filtered out. **g**, Histograms of Micro3, Astro3, Oligo2/Oligo3, OPC and neuronal cells spatial distribution around A β plaque in the TauPS2APP 8-month sample (left) and 13-month sample (right). **h**, Schematic diagram showing the spatial distribution of different cell types around A β plaque (top) and oligodendrocyte subtypes in hippocampal alveus (bottom) in the TauPS2APP mouse model. The number of cells in the schematic diagram represents the approximate ratio of cell number for each cell type.



Analysis framework

In a mouse model of AD exhibiting amyloidosis, tauopathy and neurodegeneration, we applied this high-resolution and multimodal *in situ* mapping with four computational analysis strategies to identify disease-associated cell populations and gene programs as follows: (1) hierarchical cell clustering analysis to pinpoint disease-associated cell subtypes, (2) pseudotime trajectory analysis to reconstruct the transitions of cell states during disease progression, (3) spatial analysis to recognize changes in cell types and cell states in physical proximity of A β plaques and tauopathy; (4) differential gene expression analysis in spatiotemporal relationship with amyloid and p-tau and disease stage to identify disease-associated gene pathways. This analysis framework successfully traced how AD hallmark pathologies correlate with gene pathways that drive inflammation, gliogenesis and neurodegeneration across different cell types. Because STARmap PLUS is a targeted analysis based on a curated gene list (2,766 genes in this study), it may not fully capture all disease-associated biological pathways and gene markers.

Core–shell structures surrounding plaques

Applying our methods to the TauPS2APP mouse AD model at two different ages, we have constructed a cell type and cell state resolved spatiotemporal map of the TauPS2APP mouse model (Fig. 7g,h). Specifically, in response to the emergence of A β plaques (at 8 months or earlier), microglia are the primary responders, closely aggregating around plaques (<10 μ m distance away from plaques; Fig. 7g,h). Integrative spatial and pseudotime analysis of microglia subtypes suggests a cell state transition from Micro1 and Micro2 to Micro3 (DAM) subtype in microglia cells accumulating around A β plaques (Fig. 3 and Extended Data Fig. 4). The transition from Astro2 to Astro3 (DAA-like) in the ring (10–30 μ m) next to the DAM microglia was seen at a later stage (13 months), indicating possible induction of DAA by DAM. Indeed, a previous study showed that reactive astrocytes with the high expression of DAA marker genes *Gfap* and *Vim* were induced by activated microglia²¹. Oligodendrocyte populations (Oligo2/Oligo3) accumulate near plaque (10–40 μ m) at a later stage (13 months) than microglia (Fig. 7g). Unexpectedly, we discovered that OPCs were enriched in the region 10–30 μ m from plaques at 8- and 13-month stages, indicating potential *in situ* proliferation and differentiation of OPCs to oligodendrocytes at intermediate distance from plaque. In contrast to the accumulation of glia, neuron density around plaque declined progressively from 8 to 13 months (Fig. 7g,h).

Based on the collective data, we propose a core–shell structure of glial cells surrounding A β plaques where the DAM emerge early in disease near plaques as the core, and the shell is a gliogenesis zone enriched for DAA-like cells, OPC and oligodendrocytes that develop at a later disease stage, perhaps dependent on the formation of the inner ring of reactive microglia. Because STARmap PLUS only captures snapshots from different disease stages, the dynamic cell type and state transitions inferred from pseudotime trajectory reconstruction and spatial patterns need future verification by live-cell imaging or *in vivo* cell-fate tracing approaches.

Oligodendrocytes and tauopathy

In the TauPS2APP model, hyperphosphorylated tau (as detected with AT8 antibody) was mainly found in CA1 excitatory neuronal bodies and its upper layer of axon tracts (alveus), where it is strongly associated with oligodendrocyte subtypes regardless of the presence or absence of plaques (schematized in Fig. 7h). It is unclear whether the enrichment of oligodendrocytes is a reactive mechanism to support tauopathy-injured axons, repair damaged myelin, or whether oligodendrocytes instead exacerbate tauopathy. It is possible that oligodendrocyte subtypes might feature distinct responses and exert different impacts; for example, Oligo1 is homeostatic and protective while Oligo2 or Oligo3 is detrimental in response to tau-driven changes. The reciprocal functional interactions between oligodendrocytes and

neurons (beyond oligodendrocytes providing electrical insulation and metabolic support for axons) are increasingly appreciated and studied⁵³. Single-cell RNA-seq studies of human AD brain tissues have noted major transcriptomic changes in oligodendrocytes, but without spatial information in relation to plaque and p-tau¹². Enabled by high-resolution spatial transcriptomic analysis of oligodendrocytes in the TauPS2APP mice, we identified oligodendrocyte subtypes that are associated with tauopathy. Further pathway analysis implicated oligodendrocyte DEGs in myelination and axon ensheathment (Extended Data Fig. 7g), pointing to a potential correlation between axonal tauopathy and oligodendrocytes.

Implications for neurodegeneration mechanisms in AD

The overall density of neuronal cells in the cortex declines near A β plaques (Fig. 6g,h), implying neurotoxicity or physical exclusion due directly to A β aggregation or indirectly via the effects of amyloid on microglia and other glia surrounding the plaque. This notion is supported by the accumulation of p-tau in dystrophic neurites near to plaque, which we confirmed with STARmap PLUS. We cannot exclude that neurons are merely crowded out from plaque-adjacent regions by reactive glia; however, we note that the TauPS2APP mice show macroscopic brain volume loss by 13 months of age⁴⁰ and reduced synapse density around plaques by 17 months of age⁵⁴. Further consistent with a neuronal loss around plaques, we note that neurons in DG, where a large amount of A β plaques appeared by 13 months, showed altered transcriptional profile in the regulation of neuron projection development and molecular pathways related to synapse structure and organization. Meanwhile, all neuronal types examined in the cortex and hippocampus of TauPS2APP share some common DEGs (that is, *Ccnb2* and *Ddit3*) that might suggest a general mechanism of neurodegeneration across neuronal cell types. By simultaneous transcriptomic profiling and immunostaining in STARmap PLUS, we observed that most of the p-tau⁺ inhibitory neurons in 13-month TauPS2APP mice belong to the Sst interneuron subtype, which may be related to the observation that Sst neurons are more vulnerable to tauopathy than other neuronal types in human AD patients⁵⁵. The core–shell glial structure around plaques implies potential microglial crosstalk with astrocytes²¹ and oligodendrocytes. Different subtypes of the oligodendrocyte lineage respond differently to plaques and tauopathy, suggesting distinct modes of oligodendrocyte recruitment and reactivity (for example, microglia-oligodendrocyte/OPC interactions near plaques and neuron-oligodendrocyte interactions in tauopathy). Future studies in human patient samples and other AD disease models are needed to test the potential pathogenic mechanisms revealed by STARmap PLUS analysis of the TauPS2APP mouse brains.

Online content

Any methods, additional references, Nature Portfolio reporting summaries, source data, extended data, supplementary information, acknowledgements, peer review information; details of author contributions and competing interests; and statements of data and code availability are available at <https://doi.org/10.1038/s41593-022-01251-x>.

References

1. Masters, C. L. et al. Alzheimer's disease. *Nat. Rev. Dis. Prim.* **1**, 15056 (2015).
2. Braak, H. & Braak, E. Neuropathological stageing of Alzheimer-related changes. *Acta Neuropathol.* **82**, 239–259 (1991).
3. Busche, M.A. & Hyman, B.T. Synergy between amyloid- β and tau in Alzheimer's disease. *Nat. Neurosci.* **23**, 1183–1193 (2020).
4. Hardy, J. & Selkoe, D. J. The amyloid hypothesis of Alzheimer's disease: progress and problems on the road to therapeutics. *Science* **297**, 353–356 (2002).
5. Beach, T. G., Walker, R. & McGeer, E. G. Patterns of gliosis in Alzheimer's disease and aging cerebrum. *Glia* **2**, 420–436 (1989).

6. Butt, A. M., De La Rocha, I. C. & Rivera, A. Oligodendroglial cells in Alzheimer's disease. *Adv. Exp. Med. Biol.* **1175**, 325–333 (2019).
7. Henstridge, C. M., Hyman, B. T. & Spires-Jones, T. L. Beyond the neuron–cellular interactions early in Alzheimer disease pathogenesis. *Nat. Rev. Neurosci.* **20**, 94–108 (2019).
8. Grubman, A. et al. A single-cell atlas of entorhinal cortex from individuals with Alzheimer's disease reveals cell-type-specific gene expression regulation. *Nat. Neurosci.* **22**, 2087–2097 (2019).
9. Habib, N. et al. Disease-associated astrocytes in Alzheimer's disease and aging. *Nat. Neurosci.* **23**, 701–706 (2020).
10. Keren-Shaul, H. et al. Unique microglia type associated with restricting development of Alzheimer's disease. *Cell* **169**, 1276–1290 (2017).
11. Lau, S.-F., Cao, H., Fu, A. K. Y. & Ip, N. Y. Single-nucleus transcriptome analysis reveals dysregulation of angiogenic endothelial cells and neuroprotective glia in Alzheimer's disease. *Proc. Natl Acad. Sci. USA* **117**, 25800–25809 (2020).
12. Mathys, H. et al. Single-cell transcriptomic analysis of Alzheimer's disease. *Nature* **570**, 332–337 (2019).
13. Zhou, Y. et al. Human and mouse single-nucleus transcriptomics reveal TREM2-dependent and TREM2-independent cellular responses in Alzheimer's disease. *Nat. Med.* **26**, 131–142 (2020).
14. Bohlen, C. J., Friedman, B. A., Dejanovic, B. & Sheng, M. Microglia in brain development, homeostasis, and neurodegeneration. *Annu. Rev. Genet.* **53**, 263–288 (2019).
15. Deczkowska, A. et al. Disease-associated microglia: a universal immune sensor of neurodegeneration. *Cell* **173**, 1073–1081 (2018).
16. Friedman, B. A. et al. Diverse brain myeloid expression profiles reveal distinct microglial activation states and aspects of Alzheimer's disease not evident in mouse models. *Cell Rep.* **22**, 832–847 (2018).
17. Hansen, D. V., Hanson, J. E. & Sheng, M. Microglia in Alzheimer's disease. *J. Cell Biol.* **217**, 459–472 (2018).
18. Lewcock, J. W. et al. Emerging microglia biology defines novel therapeutic approaches for Alzheimer's disease. *Neuron* **108**, 801–821 (2020).
19. Masuda, T., Sankowski, R., Staszewski, O. & Prinz, M. Microglia heterogeneity in the single-cell era. *Cell Rep.* **30**, 1271–1281 (2020).
20. Clarke, L. E. et al. Normal aging induces A1-like astrocyte reactivity. *Proc. Natl Acad. Sci. USA* **115**, E1896–E1905 (2018).
21. Liddelow, S. A. et al. Neurotoxic reactive astrocytes are induced by activated microglia. *Nature* **541**, 481–487 (2017).
22. Liddelow, S. A. & Barres, B. A. Reactive astrocytes: production, function, and therapeutic potential. *Immunity* **46**, 957–967 (2017).
23. Shi, Y. et al. ApoE4 markedly exacerbates tau-mediated neurodegeneration in a mouse model of tauopathy. *Nature* **549**, 523–527 (2017).
24. Sofroniew, M. V. Astrocyte reactivity: subtypes, states, and functions in CNS innate immunity. *Trends Immunol.* **41**, 758–770 (2020).
25. Yun, S. P. et al. Block of A1 astrocyte conversion by microglia is neuroprotective in models of Parkinson's disease. *Nat. Med.* **24**, 931–938 (2018).
26. van den Brink, S. C. et al. Single-cell sequencing reveals dissociation-induced gene expression in tissue subpopulations. *Nat. Methods* **14**, 935–936 (2017).
27. Thrupp, N. et al. Single-nucleus RNA-seq is not suitable for detection of microglial activation genes in humans. *Cell Rep.* **32**, 108189 (2020).
28. Marsh, S. E. et al. Dissection of artifactual and confounding glial signatures by single-cell sequencing of mouse and human brain. *Nat. Neurosci.* **25**, 306–316 (2022).
29. Bennett, F. C. et al. A combination of ontogeny and CNS environment establishes microglial identity. *Neuron* **98**, 1170–1183 (2018).
30. Chen, K. H., Boettiger, A. N., Moffitt, J. R., Wang, S. & Zhuang, X. RNA imaging. Spatially resolved, highly multiplexed RNA profiling in single cells. *Science* **348**, aaa6090 (2015).
31. Rodrigues, S. G. et al. Slide-seq: a scalable technology for measuring genome-wide expression at high spatial resolution. *Science* **363**, 1463–1467 (2019).
32. Stähli, P. L. et al. Visualization and analysis of gene expression in tissue sections by spatial transcriptomics. *Science* **353**, 78–82 (2016).
33. Stuart, T. & Satija, R. Integrative single-cell analysis. *Nat. Rev. Genet.* **20**, 257–272 (2019).
34. Wang, X. et al. Three-dimensional intact-tissue sequencing of single-cell transcriptional states. *Science* **361**, eaat5691 (2018).
35. Qian, X. et al. Probabilistic cell typing enables fine mapping of closely related cell types in situ. *Nat. Methods* **17**, 101–106 (2020).
36. Alon, S. et al. Expansion sequencing: spatially precise in situ transcriptomics in intact biological systems. *Science* **371**, eaax2656 (2021).
37. Liu, S. et al. Barcoded oligonucleotides ligated on RNA amplified for multiplexed and parallel in situ analyses. *Nucleic Acids Res.* **49**, e58 (2021).
38. Chen, W.-T. et al. Spatial transcriptomics and in situ sequencing to study Alzheimer's disease. *Cell* **182**, 976–991 (2020).
39. Grueninger, F. et al. Phosphorylation of tau at S422 is enhanced by A β in tauPS2APP triple transgenic mice. *Neurobiol. Dis.* **37**, 294–306 (2010).
40. Lee, S.-H. et al. Trem2 restrains the enhancement of tau accumulation and neurodegeneration by β -amyloid pathology. *Neuron* **109**, 1283–1301 (2021).
41. Lein, E., Borm, L. E. & Linnarsson, S. The promise of spatial transcriptomics for neuroscience in the era of molecular cell typing. *Science* **358**, 64–69 (2017).
42. Koopmans, F. et al. SynGO: an evidence-based, expert-curated knowledge base for the synapse. *Neuron* **103**, 217–234 (2019).
43. Lambert, J. C. et al. Meta-analysis of 74,046 individuals identifies 11 new susceptibility loci for Alzheimer's disease. *Nat. Genet.* **45**, 1452–1458 (2013).
44. Saunders, A. et al. Molecular diversity and specializations among the cells of the adult mouse brain. *Cell* **174**, 1015–1030 (2018).
45. Yao, Z. et al. A taxonomy of transcriptomic cell types across the isocortex and hippocampal formation. *Cell* **184**, 3222–3241 (2021).
46. Zamani, J. L. et al. Genomic analysis of reactive astrogliosis. *J. Neurosci.* **32**, 6391–6410 (2012).
47. Zeisel, A. et al. Molecular architecture of the mouse nervous system. *Cell* **174**, 999–1014 (2018).
48. Cao, J. et al. The single-cell transcriptional landscape of mammalian organogenesis. *Nature* **566**, 496–502 (2019).
49. Feregrino, C. & Tschopp, P. Assessing evolutionary and developmental transcriptome dynamics in homologous cell types. *Dev. Dyn.* **251**, 1472–1489 (2022).
50. Moreno-Jiménez, E. P. Adult hippocampal neurogenesis is abundant in neurologically healthy subjects and drops sharply in patients with Alzheimer's disease. *Nat. Med.* **25**, 554–560 (2019).
51. Raudvere, U. et al. g:Profiler: a web server for functional enrichment analysis and conversions of gene lists (2019 update). *Nucleic Acids Res.* **47**, W191–W198 (2019).
52. Shannon, P. et al. Cytoscape: a software environment for integrated models of biomolecular interaction networks. *Genome Res.* **13**, 2498–2504 (2003).
53. Pease-Raissi, S. E. & Chan, J. R. Building a (w)rapport between neurons and oligodendroglia: reciprocal interactions underlying adaptive myelination. *Neuron* **109**, 1258–1273 (2021).
54. Dejanovic, B. et al. Complement C1q-dependent excitatory and inhibitory synapse elimination by astrocytes and microglia in Alzheimer's disease mouse models. *Nat. Aging* **2**, 837–850 (2022).

55. Cain, A. et al. Multi-cellular communities are perturbed in the aging human brain and with Alzheimer's disease. Preprint at *bioRxiv*. <https://doi.org/10.1101/2020.12.22.424084> (2020).

Publisher's note Springer Nature remains neutral with regard to jurisdictional claims in published maps and institutional affiliations.

Springer Nature or its licensor (e.g. a society or other partner) holds exclusive rights to this article under a publishing agreement with the author(s) or other rightsholder(s); author self-archiving of the accepted manuscript version of this article is solely governed by the terms of such publishing agreement and applicable law.

© The Author(s), under exclusive licence to Springer Nature America, Inc. 2023

Methods

Mice

All animal procedures followed animal care guidelines approved by the Genentech Institutional Animal Care and Use Committee (IACUC), and animal experiments were conducted in compliance with IACUC policies and NIH guidelines. The mice used for STARmap PLUS include the pR5-183 line expressing the P301L mutant of human tau and PS2_{N141} and APP_{swe} (PS2APP^{homo}; P301L^{hemi}, termed as ‘TauPS2APP’ in the current study) and nontransgenic control (termed as ‘control’ in the current study). Animals were housed in specific pathogen-free conditions with 12 h light/12 h dark lighting and maintained on a regular chow diet. For 2,766 gene experiments, two 8-month TauPS2APP male mice, two 8-month control male mice, two 13-month TauPS2APP male mice and two 13-month control male mice were used. For the 64 gene validation experiment, one 8-month TauPS2APP male mouse, one 8-month control male mouse, one 13-month TauPS2APP male mouse and one 13-month control male mouse were used. No statistical methods were used to predetermine sample sizes, but our sample sizes are similar to those reported in previous publications^{9,38}.

Tissue collection and sample preparation for STARmap PLUS

Animals were anesthetized with isoflurane and rapidly decapitated. Brain tissue was removed, placed in O.C.T., then frozen in liquid nitrogen and kept at -80 °C. For the tissue sectioning, mouse brains were transferred to cryostat (Leica CM1950) and cut into 20 µm thick slices in coronal sections at -20 °C. The slices were attached to each well of glass-bottom 12-well plates pretreated by methacryloxypropyltrimethoxysilane (bind-silane) and poly-D-lysine. The brain slices were fixed with 4% PFA in 1× PBS buffer at room temperature for 15 min, then permeabilized with -20 °C methanol and placed at -80 °C for an hour before hybridization.

STARmap PLUS to detect spatial RNA and protein signals

The samples were taken from -80 °C to room temperature for 5 min and then washed with PBSTR buffer (0.1% Tween-20, 0.1 U µl⁻¹ SUPERase-In RNase Inhibitor in PBS). After washing, the samples were incubated with 300 µl of 1× hybridization buffer (2× SSC, 10% formamide, 1% Tween-20, 0.1 mg ml⁻¹ yeast tRNA, 20 mM ribonucleoside vanadyl complexes, 0.1 U µl⁻¹ SUPERase-In RNase Inhibitor and pooled SNAIL probes (ordered from IDT) at 1 nM per oligo) in a 40 °C humidified oven with shaking and parafilm wrapping for 36 h. The samples were washed by PBSTR twice and high-salt washing buffer (4× SSC dissolved in PBSTR) once at 37 °C. Finally, the samples were rinsed with PBSTR once at room temperature. The samples were then incubated with a ligation mixture (1:10 dilution of T4 DNA ligase in 1× T4 DNA ligase buffer supplemented with 0.5 mg ml⁻¹ BSA and 0.2 U µl⁻¹ of SUPERase-In RNase inhibitor) at room temperature for 2 h with gentle shaking. After ligation, the samples were washed twice with PBASR buffer and then incubated with rolling circle amplification mixture (1:10 dilution of Phi29 DNA polymerase in 1× Phi29 buffer supplemented with 250 µM dNTP, 20 µM 5-(3-aminoallyl)-dUTP, 0.5 mg ml⁻¹ BSA and 0.2 U µl⁻¹ of SUPERase-In RNase inhibitor) at 30 °C for 2 h with gentle shaking. Subsequently, the samples were washed twice with PBST (0.1% Tween-20 in PBS) and blocked with blocking solution (5 mg ml⁻¹ BSA in PBST) at room temperature for 30 min. The samples were then incubated with Phospho-Tau (Ser202, Thr205) Antibody (Thermo, MN1020B; 1:100 dilution in blocking solution) and anti-GFAP Antibody (only for 64 gene samples; Abcam, ab4674; 1:500 dilution in blocking solution) or 2 h at room temperature. The samples were washed with PBST three times for 5 min each. Next, the samples were treated with 20 mM Acrylic acid NHS ester in PBST for 1 h and rinsed once with PBST. The samples were incubated in the monomer buffer (4% acrylamide and 0.2% bis-acrylamide in 2× SSC) for 15 min at room temperature. Then the buffer was aspirated, and a 35 µl polymerization mixture (0.2% ammonium persulfate and 0.2% tetramethylethylenediamine dissolved in monomer buffer) was

added to the center of the sample and immediately covered by Gel Slick-coated coverslip. The polymerization reaction was undergone for 1 h at room temperature (N₂) and washed by PBST twice for 5 min each. Subsequently, the samples were treated with dephosphorylation mixture (1:100 dilution of Shrimp Alkaline Phosphatase in 1× CutSmart buffer supplemented with 0.5 mg ml⁻¹ BSA) at 37 °C for 1 h and washed by PBST three times for 5 min each.

For SEDAL sequencing, each cycle began with treating the sample with stripping buffer (60% formamide and 0.1% Triton-X-100 in H₂O) at room temperature for 10 min twice, followed by PBST washing three times, 5 min each. The sample was incubated with a sequencing mixture (1:25 dilution of T4 DNA ligase in 1× T4 DNA ligase buffer supplemented with 0.5 mg ml⁻¹ BSA, 10 µM reading probe and 5 µM fluorescent oligos) at room temperature for at least 3 h. The samples were washed by washing and imaging buffer (10% formamide in 2× SSC) three times, 10 min each, then immersed in washing and imaging buffer for imaging.

Images were acquired using Leica TCS SP8 confocal microscopy (Leica LAS-X microscope imaging software) with a 405 nm diode, a white light laser, and a ×40 oil immersion objective (NA1.3). The laser lines we used for SEDAL sequencing are ALEXA 488 nm, ALEXA 546 nm, ALEXA 594 nm and ALEXA 647 nm. We imaged 56–64 FOVs for each sample with a voxel size of 95 nm (x axis) × 95 nm (y axis) × 350 nm (z axis) and 30 z slices (10 µm in total). Eight cycles of imaging were performed to detect 2,766 genes.

After eight-round *in situ* sequencing for 2,766 gene samples and four-round *in situ* sequencing for 64 gene samples, the sample was incubated in X-34 solution (10 µM X-34, 40% ethanol and 0.02 M NaOH in 1× PBS) at room temperature for 10 min, followed by quick washing with 1× PBS for three times. The samples were incubated with 80% EtOH for 1 min and then washed with PBS 3 times, 1 min each. Then the samples were incubated with the goat anti-mouse IgG (H+L) Cross-Adsorbed Secondary Antibody, Alexa Fluor 488 (Thermo, A-11001; 1:80 dilution in blocking solution) and goat anti-chicken IgY (H+L) Cross-Adsorbed Secondary Antibody, Alexa Fluor Plus 647 (only for 64 gene samples; Thermo, A32933; 1:80 dilution in blocking solution) at room temperature for 12 h. The sample was washed three times with PBST for 5 min each. The samples were incubated with the 500 nM 19-nt fluorescent oligo complementary to DNA amplicon in PBST (only for 2,766 gene samples) at room temperature for 1 h, then washed by PBST three times for 5 min each. Propidium iodide (PI) staining was performed following the manufacturer’s instructions for the purpose of cell segmentation. Another round of imaging with the same resolution as the SEDAL sequencing was performed to detect spatial protein signals. The data collection was not randomized, as we needed to image TauPS2APP sample before the control sample (which showed no plaque and p-tau signal) to make sure the laser intensity was set up suitable. Data collection and analysis were not performed blind to the conditions of the experiments. No animals or data points were excluded from the analyses.

STARmap PLUS image processing

All of the image processing steps were implemented using MATLAB R2019b and related open-source packages in Python 3.6 and applied according to (ref. ³⁴).

Image preprocessing and registration. First, the illuminance and contrast level of images were unified with a multidimensional histogram matching by MATLAB function ‘imhistmatchn’. Then, customized tophat filtering was applied to the sequencing images to further enhance the signal and suppress the background noise. Image registration was applied according to (ref. ³⁴). Global image registration was accomplished using a 3D fast Fourier transform to compute the cross-correlation between two image volumes at all translational offsets. The position of the maximal correlation coefficient was identified and used to translate image volumes to compensate for the offset.

Then a nonrigid registration was applied with MATLAB function ‘imregdemons’ to further align images in different sequencing rounds.

Spot calling. After registration, individual dots were identified separately in each color channel on the first round of sequencing. Amplicon dots were identified by finding local maxima in 3D with MATLAB function ‘imregionalmax’. Intensity threshold was applied to exclude dim dots. Because the dot was approximately six pixels in diameter on the xy plane, the dominant color for that dot across all four channels on each round was determined by a $5 \times 5 \times 3$ voxel volume surrounding the dot centroid. The integrated intensity of the voxel volume in each channel was used for color determination. In this case, each dot in each round had an L2 normalized vector with four elements. The color of each dot was determined by the corresponding channel with the highest value in the vector. Dots with multiple maximum values in the vector were discarded.

Barcode filtering. Dots were first filtered based on the quality scores (average of $-\log$ (color vector value in the dominant channel) across all sequencing rounds). The quality score quantified the extent to which each dot on each sequencing round came from one color rather than a mixture of colors. The barcode codebook was converted into color space based on the expected color sequence following the 2-base encoding of the barcode DNA sequence. Dot color sequences that passed the quality threshold and matched sequences in the codebook were kept and identified with the specific gene that that barcode represented; all other dots were rejected. The high-quality dots and associated gene identities in the codebook were then saved for downstream analysis.

2D cell segmentation. Nuclei were automatically identified by applying a pretrained 2D machine learning model from the StarDist package⁵⁶ to a sum intensity projection of the stitched PI channel following the final round of sequencing. Then the cell locations were extracted from the segmented PI image and used as markers for cell body segmentation. Cell bodies were represented by an overlay of stitched PI staining and merged amplicon images. A gaussian filter with σ equal to ten was applied to the composite image and the image was then binarized with Otsu thresholding strategy. To better incorporate the amplicons around the peripheral region of cell bodies, a binary dilation with a disk structure element ($r=10$) was applied on the mask. Finally, a marker-based watershed transform was performed to segment the binary mask representing cell bodies. Points overlapping each segmented cell region in 2D were then assigned to that cell, to compute a per-cell gene expression matrix.

Protein image preprocessing. p-tau images were processed using a customized Fiji macro⁵⁷. A rolling ball background subtraction with a radius equal to five was applied to each image. Then each image was processed with a Gaussian filter with a σ value equal to two and followed by a maximum entropy binarization.

Cell type classification

A two-level clustering strategy was applied to identify both major and sublevel cell types in the dataset. Processing steps in this section were implemented using Scanpy v1.4.6 (ref. ⁵⁸) and other customized scripts in Python 3.6 and applied according to (ref. ³⁴). A standardized preprocessing pipeline was first performed on the single-cell gene expression matrix including filtering, normalization and scaling. Given that the biological replicates were collected in two batches, a batch correction process was applied with the ComBat method⁵⁹ implemented in Scanpy. Genes with the maximum count less than two per cell were excluded in the following process to achieve a high-quality gene expression library. A PCA was applied to reduce the dimensionality of the cellular expression matrix. The top 30 PCs were used to compute a kNN graph of the

observations. The Leiden community detection algorithm was applied over the kNN graph to detect cell clusters. Clusters were annotated based on their top representative markers. Then, they were displayed using the UMAP and diffusion map embeddings where each cluster was color-coded according to its cell type annotation. The cells for each interested top-level cluster were then extracted and subclustered again.

Subtype identification

Microglia, astrocyte, oligodendrocyte and neuron populations identified from the previous unsupervised clustering were extracted and the PCA was applied to the preprocessed gene expression profile of each population to compute top PCs respectively. For astrocytes, a modified preprocessing pipeline was used to further minimize the influence of ambient transcripts signal. In detail, genes were filtered based on their expression percentage within each major cell population. Genes expressed by less than 5% of all astrocytes were excluded and genes expressed by more than 85% of cells from other major cell types were also excluded from astrocytes’ expression profiles. The filtered gene expression matrix was then corrected by ComBat to account for the variance from experiment batches. Then, the variance from the total number of transcripts per cell was regressed out. After PCA, significant principal components were identified using the elbow method. The PCs were also used for diffusion map modeling with the function ‘tl.diffmap’. Again, a kNN graph was built with the significant PCs of each population and the Leiden community detection algorithm was applied over the kNN graph to detect cell clusters. Clusters were then annotated according to their representative gene markers and further visualized on UMAP and diffusion map embeddings.

Comparison with other datasets from integration

To further interpret and validate the disease-associated subpopulations identified, a canonical correlation analysis-based integration and label transfer were conducted with the Seurat package (v4.0.2) in R⁶⁰. Two different single-nucleus transcriptome datasets from AD human patients and 5xFAD mouse model were used as integration references to label cells from STARmap PLUS^{9,12}. In detail, the count matrix of the human microglia and astrocytes were obtained from (ref. ¹²) with provided cell annotations. The gene expression matrixes were normalized and scaled by related functions within the Seurat package⁶⁰. Genes from the STARmap PLUS dataset were first mapped to human genes¹². Then, the intersection between the mapped genes and the top 2,000 most variable genes from the corresponding human cell populations was used in the integration process. Each cell from the STARmap PLUS dataset got assigned a subcluster label from the human data. Cells with a prediction score higher than the overall median value were kept and further visualized (Extended Data Figs. 4b,c and 5e,f). Label transfer of the 5xFAD mice snRNA-seq dataset was achieved in the same manner as the process of human data but only with astrocytes of 7-month-old male mice in (ref. ⁹) (Extended Data Fig. 5g,h).

Pseudotime and trajectory analysis

An R package Monocle3 (ref. ⁴⁸, <https://cole-trapnell-lab.github.io/monocle3/>) was utilized for pseudotime calculation. Monocle3 firstly learned a principal graph (via *learn_graph* function) in the 2D diffusion map space using a dimensionality reduced representation of original data. Then, to compute pseudotime from the principal graph, the root node(s) must be specified by the user, and the pseudotime for each cell can be assigned by calculating the geodesic distance from root node to the cell node along the principal graph. In this case, the roots used in inference were chosen based on the spot/area in the embedding space that was occupied by cells from early time points (8 months) in the control sample as they were the cells in a relatively homeostatic state. The raw expression matrix of each cell type, Microglia, Astrocyte and Oligodendrocyte (OPC), was used separately as the input of Monocle3. To visualize the results, we used the original Diffusion map embedding

with palettes representing normalized pseudotime (rescaled to 0–1), cell types and sample identities.

Spatial analysis

Plaque segmentation. First, a gaussian filter with σ equal to two was applied to the stitched images of the plaque channel. The filtered images were binarized with an intensity threshold equal to 30. The plaques were segmented from the binarized image of the plaque channel by using the ‘bwlabel’ function in EBImage package⁶¹. Then, the size and the center of each plaque were calculated by using ‘computeFeatures.moment’ and ‘computeFeatures.shape’ functions respectively. Finally, plaques with an area greater than 400 pixels ($\sim 40 \mu\text{m}^2$) were kept for the downstream analysis.

Cell composition around plaques. As filtered plaques were acquired in the last step, we dilated the plaque images 5 times with steps of 10 microns. Next, we counted the number of cells for every cell type that fall into different intervals. The ranges were set from 0–10 μm (Ring 1) to 40–50 μm (Ring 5). The statistics were normalized by calculating the percentage and density of each cell type in a ring. The graphical explanation of this analysis is shown in Fig. 2d. For the overall statistics, we calculated the percentage and density of each cell type in the whole sample. To test the significance of cell enrichment in both density and proportion aspects in specific intervals, two kinds of statistical tests, one-sample *t*-test and chi-square test (Fisher’s exact test), were utilized. One-sample *t*-test was used to compare the density values for each cell type in one interval around every plaque with the average density and the data met the assumptions of the statistical tests used. According to the difference between mean value of the density sequence and the average density, an alternative hypothesis was set correspondingly to test whether the density was substantially higher or lower. For the chi-square test, raw cell counts in each interval were used for the test.

Differential expression analysis

Before performing DE analysis, the dataset was normalized according to the following steps: (1) divide the gene counts in a sample by the median of total counts per cell for that sample and multiply by the scale factor, which was defined as the mean value of median of *total counts per cell* for all samples; (2) Perform log₂ transformation by adding a pseudo-count of one. DE genes were identified by performing Wilcoxon rank-sum test between two groups of cells using the ‘FindMarkers’ function in Seurat⁶⁰. For the ‘disease versus control’ comparison of specific cell types, the two groups of cells were extracted from TauPS2APP and control samples and compared. In the comparison of ‘CA1 tau⁺ vs. tau⁻’, tau⁺ CA1 cells were defined according to the fraction of tau signal area to the cell body’s area. The threshold was set to 0.07.

To filter out lowly expressed genes, genes that were expressed by less than 5% of cells in either group of the comparison were excluded. We also applied the following threshold values on the generated gene list to filter out nonsignificant genes: absolute values of log fold change >0.1 , $P < 0.05$.

To visualize the DE result, we used the ‘EnhancedVolcano’ package (<https://github.com/kevinblighe/EnhancedVolcano>) to generate the volcano plot. DE genes with $\log_{2}\text{FC} > 0$ were colored in red while others were colored in blue. Those significant genes ($P < 0.05$) that failed to pass the $\log_{2}\text{FC}$ threshold were green-tinted. All other nonsignificant genes were colored in gray. Note, some genes with extremely high $-\log(P\text{value})$ or $\log_{2}\text{FC}$ were capped.

Pathway analysis using gProfiler

The R client of gProfiler (gprofiler2 package v0.1.9) was used to perform pathway analysis for each cell type with a significant (absolute $\log_{2}\text{FC} > 0.1$, $P < 0.05$) DE gene list whose genes were detected in a minimum fraction of 5% cells in the targeted cell type. Gene Ontology Biological Processes (GO:BP, using the default data source provided by

gProfiler) database was selected as the gene sets database to perform gProfiler analysis. To limit the size of gene sets subjected to enrichment analysis, the minimum and maximum sizes of gene sets were set to 10 and 1,000, respectively. The enriched terms were selectively visualized using bar plot with their $-\log_{10}(P\text{value})$. The SynGO enrichment tool⁴² was used to further characterize the synapse functions enriched in DEGs from Dentate gyrus and CA1 cells with tau pathology. Brain-expressed genes were used as the background gene list.

Grid analysis

To analyze the scattered p-tau signal, the p-tau images were first segmented by a 20 μm grid (see heatmap in Extended Data Fig. 5f). For each block, we counted the number of cells for each major cell type and the overall p-tau signal intensity. Based on the distribution of p-tau intensity and the existence of plaque, blocks were classified into four groups: no p-tau, low p-tau (intensity of p-tau in 1–50% range of population with nonzero p-tau signal), high p-tau w/plaque (51–100% range with plaque) and high p-tau w/o plaque (51–100% range without plaque). The significance of cell type enrichment was tested using one-sample *t*-test comparing the density values of each group with average density.

SDEGs analysis

To identify potential gene expression patterns around plaque for all cells, we first calculated the average expression value for each gene in five intervals as follows: 0–10 μm , 10–20 μm , 20–30 μm , 30–40 μm and $>40 \mu\text{m}$. The averaged expression matrix was calculated separately for disease samples in 8 and 13 months. Next, K-means clustering was applied to the matrix, respectively, and six clusters were obtained in each sample. We tested whether the averaged expression level of the cells within the high expression interval was substantially higher than that of other cells outside the interval using Wilcoxon signed-rank test (with adjusted $P < 0.05$; Supplementary Table 4). SDEGs were defined as substantially enriched genes within the 0–30 μm distance surrounding plaques (cluster 1–3). This analysis pipeline was also applied to microglia, astrocytes and oligodendrocytes to obtain cell type resolved SDEGs. For filtration, the *P* value threshold was firstly applied (Wilcoxon $P < 0.05$); besides, we expect SDEGs of astrocyte and oligodendrocyte are not enriched in the vicinity of plaques (0–10 μm) while genes with the highest expression interval at 20–30 μm are not considered as SDEGs for microglia. ‘ComplexHeatmap’ package⁶² is utilized for heatmap visualization.

Enriched GO terms analysis of SDEGs and visualization

The pathway analysis of identified SDEGs for microglia, astrocyte and OPC/oligodendrocyte followed the same procedure as described above using gProfiler (<https://biit.cs.ut.ee/gprofiler/gost>). The whole Gene Ontology database was selected as the data source for the analysis. After acquiring the enriched terms for SDEGs of each cell type, we used Cytoscape (v3.9.1) with EnrichmentMap (v3.3.1) and AutoAnnotation (v1.3.3) apps to integrate and visualize the results^{52,63}. The network was constructed using Cytoscape and EnrichmentMap with the following conservative parameters: nodes (gene sets) were reserved with *P*-adjusted values < 0.05 (gProfiler g:SCS threshold) and $q < 0.1$; the threshold for edges (representing gene similarity coefficient between gene sets) was set at 0.375. Each node was color-coded to visualize the distinctive and shared enriched terms in each cell type. The network was then clustered and annotated by AutoAnnotation (v1.3.3).

scWGCNA

We use scWGCNA, a modified WGCNA package designed to work with single-cell expression data⁴⁹, to perform weighted gene co-expression network analysis for microglia, astrocytes and oligodendrocytes. First, scWGCNA was utilized to calculate pseudo-cells to shrink the size of the dataset using the top ten PCs and ten nearest neighbors. Next, scWGCNA used only the highly variable genes to calculate the

TOM matrix with automatically selected power. The co-expression modules were then filtered by gene numbers (≥ 15) and for each cell type. The enrichment of DEGs in each gene module was calculated using FindMarkers function in Seurat.

Quantification and statistical analysis

The statistical tests and number of independent replicates per experiment are indicated in the figure legends. The statistical significance analyses of STARmap PLUS sequencing experiments are detailed in the Methods.

One-sample *t*-test was used to test the significance of cell type enrichment by comparing the density values of each cell type in each interval with average density.

Reporting summary

Further information on research design is available in the Nature Portfolio Reporting Summary linked to this article.

Data availability

The STARmap PLUS sequencing data are available on Single-Cell Portal at https://singlecell.broadinstitute.org/single_cell/study/SCP1375 and Zenodo at <https://doi.org/10.5281/zenodo.7332091>. Source data are provided with this paper.

Code availability

All code and analysis are available on GitHub at <https://github.com/wanglab-broad/mAD-analysis> and at <https://doi.org/10.5281/zenodo.7458952>.

References

56. Schmidt, U., Weigert, M., Broaddus, C. & Myers, G. *Medical Image Computing and Computer Assisted Intervention—MICCAI 2018* 265–273 (Springer International Publishing, 2018).
57. Schindelin, J. et al. Fiji: an open-source platform for biological-image analysis. *Nat. Methods* **9**, 676–682 (2012).
58. Wolf, F. A., Angerer, P. & Theis, F. J. SCANPY: large-scale single-cell gene expression data analysis. *Genome Biol.* **19**, 15 (2018).
59. Johnson, W. E., Li, C. & Rabinovic, A. Adjusting batch effects in microarray expression data using empirical Bayes methods. *Biostatistics* **8**, 118–127 (2007).
60. Hao, Y. et al. Integrated analysis of multimodal single-cell data. *Cell* **184**, 3573–3587 (2021).
61. Pau, G., Fuchs, F., Sklyar, O., Boutros, M. & Huber, W. EBImage—an R package for image processing with applications to cellular phenotypes. *Bioinformatics* **26**, 979–981 (2010).
62. Gu, Z., Eils, R. & Schlesner, M. Complex heatmaps reveal patterns and correlations in multidimensional genomic data. *Bioinformatics* **32**, 2847–2849 (2016).
63. Merico, D., Isserlin, R., Stueker, O., Emili, A. & Bader, G. D. Enrichment map: a network-based method for gene-set enrichment visualization and interpretation. *PLoS ONE* **5**, e13984 (2010).

Acknowledgements

We thank H. Shi (Broad Institute), M. Pan (Broad Institute), Q. Li (Harvard University), Z. Lin (Harvard University) and S. Wade (Broad Institute) for technical assistance, H. Xu (Peking University), Y. Zhang (Harvard University) and H. Meng (Peking University) for helpful discussions and thoughtful comments on the manuscript. X.W. acknowledges the support from the Searle Scholars Program, Thomas D. and Virginia W. Cabot Professorship, E. Scolnick Professorship, Ono Pharma Breakthrough Science Initiative Award, Merkin Institute Fellowship, Stanley Center for Psychiatric Research and NIH Director's New Innovator Award (DP2, 1DP2GM146245-01).

Author contributions

H.Z. and J.R. optimized STARmap PLUS probe design. H.Z. and Y.Z. performed STARmap PLUS experiments. J.H. and H.Z. performed computational analyses. W.L.M. prepared animal samples. H.Z., J.H., H.Z. and X.W. analyzed and interpreted the data with the inputs from W.J.M., B.D., C.J.B., S.-H.L., A.L., Z.T., H.S., J.L. and M.S. All authors contributed to writing and revising the manuscript and approved the final version. X.W. and M.S. conceptualized and supervised the project.

Competing interests

X.W., H.Z. and J.R. are inventors on pending patent applications related to STARmap PLUS. X.W. is a scientific cofounder of Stellaromics. M.S. is a scientific cofounder of Neumora and a former employee of Genentech. W.J.M., C. J. B. and S.-H.L. are present employees of Genentech. All the other authors declare no competing interests.

Additional information

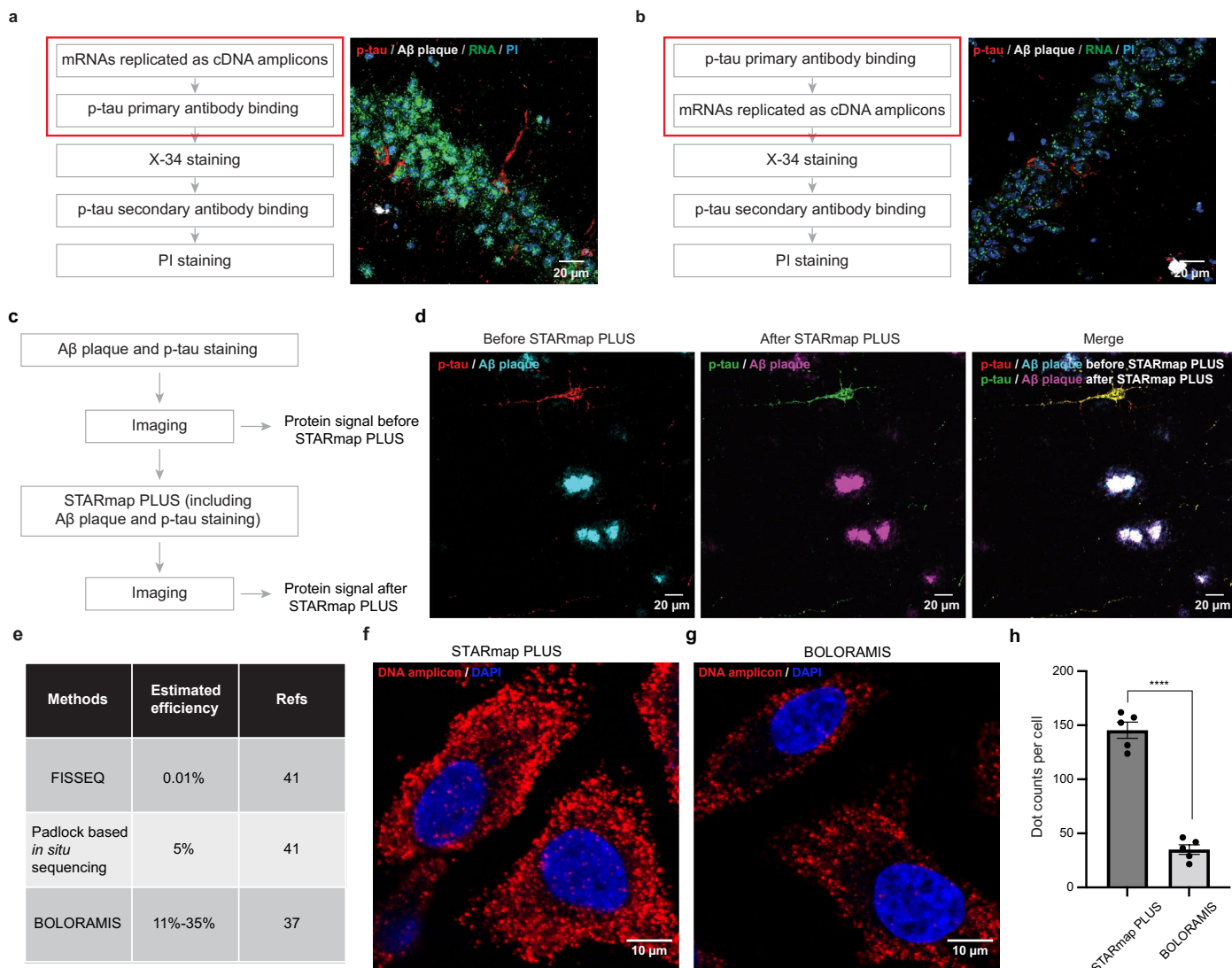
Extended data is available for this paper at <https://doi.org/10.1038/s41593-022-01251-x>.

Supplementary information The online version contains supplementary material available at <https://doi.org/10.1038/s41593-022-01251-x>.

Correspondence and requests for materials should be addressed to Morgan Sheng or Xiao Wang.

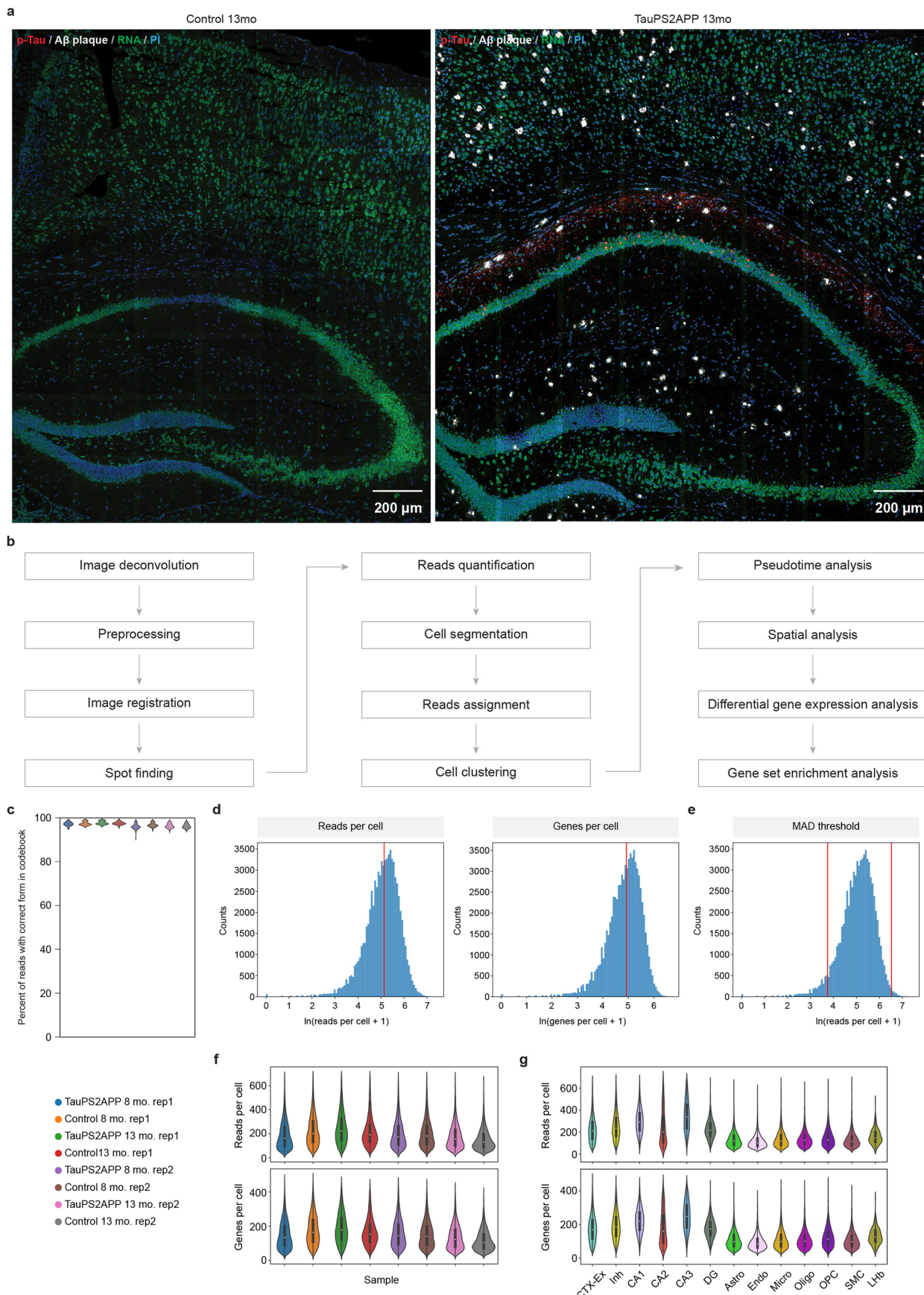
Peer review information *Nature Neuroscience* thanks Je Lee and the other, anonymous, reviewer(s) for their contribution to the peer review of this work.

Reprints and permissions information is available at www.nature.com/reprints.



Extended Data Fig. 1 | Development of the STARmap PLUS method. **a**, Flow chart of STARmap PLUS procedure where p-tau primary antibody staining was performed after mRNA *in situ* hybridization and amplification. The imaging results showed strong signals from both cDNA amplicons and proteins ($N = 2$ independent experiments). **b**, Alternative procedure where the p-tau primary antibody staining was conducted before mRNA *in situ* hybridization and amplification. The imaging results showed a much weaker signal from cDNA amplicons, suggesting RNA degradation during antibody incubation and washing steps ($N = 2$ independent experiments). PI staining, propidium iodide staining of cell nuclei. **c**, Schematic diagram of the experimental design to test if the tissue retains the same structure after STARmap PLUS. **d**, The imaging

result before STARmap PLUS (left), after STARmap PLUS (middle), and overlay (right) of p-tau and A β -plaque signals were recorded ($N = 2$ independent experiments). **e**, Summary of the detection efficiency of RCA-based spatial transcriptomics methods. The efficiency of FISSEQ and padlock based *in situ* sequencing was extracted from Lein et al.⁴¹, and the efficiency of BOLORAMIS was extracted from Liu et al.³⁷. **f,g**, The ACTB mRNA signal detected by STARmap PLUS (**f**) and BOLORAMIS³⁷ (**g**) in HeLa cells. **h**, Quantification of the number of DNA amplicons per cell identified by STARmap PLUS and BOLORAMIS. Error bars, standard deviation. Data are presented as mean \pm s.e.m., $n = 5$ images per condition. Two-sided Student's *t*-test, ***P = 1.39×10^{-6} .

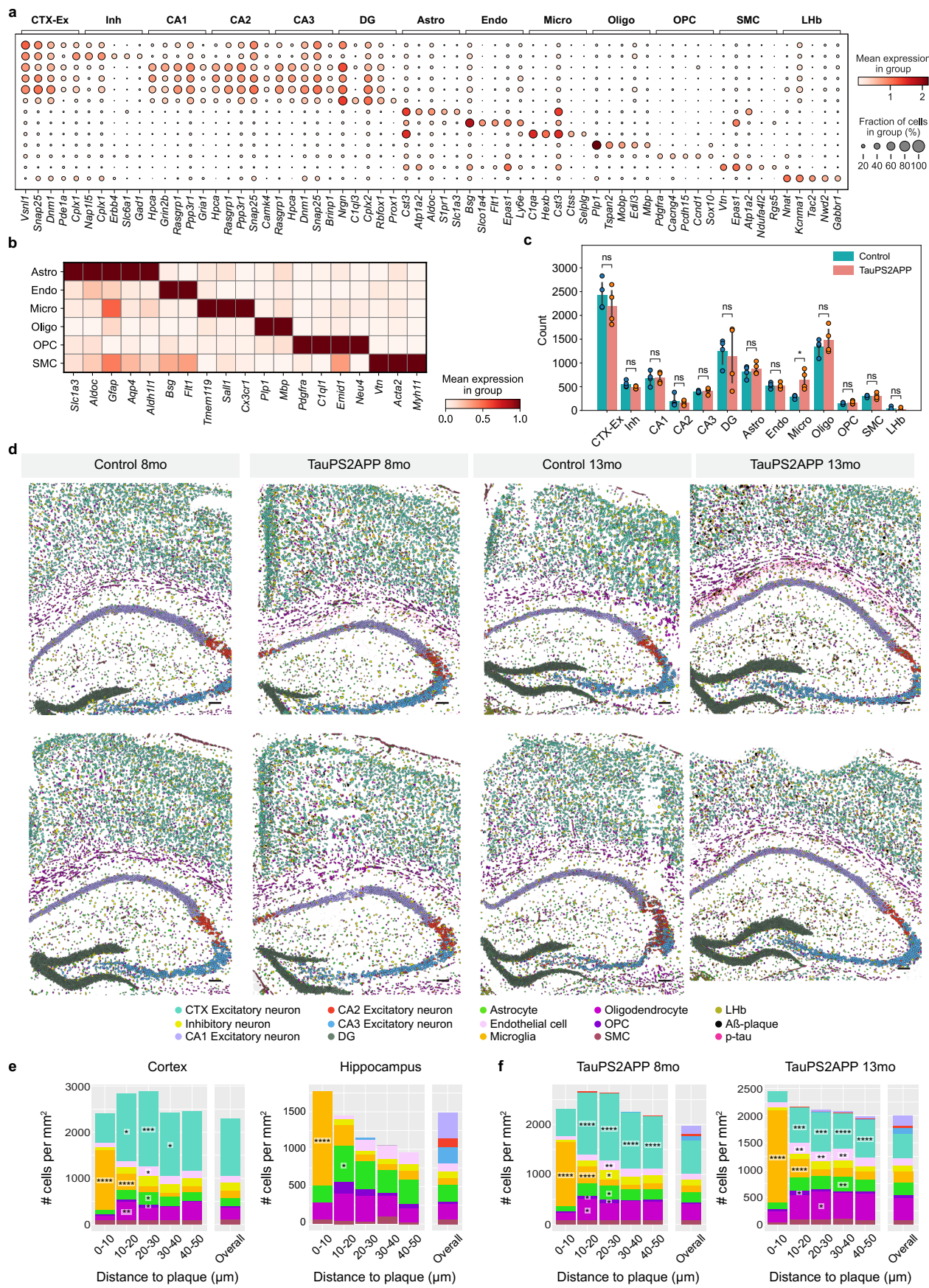


Extended Data Fig. 2 | See next page for caption.

Extended Data Fig. 2 | Data processing and quality control of the STARmap

PLUS data analysis pipeline. **a**, Examples showing the final imaging cycle detecting cell nuclei, cDNA amplicons, and protein signals in the 13-month control (left, N = 2 independent animals) and TauPS2APP (right, N = 2 independent animals) mouse brain samples. Blue, Propidium Iodide (PI) staining of cell nuclei. Green, fluorescent DNA probe staining of all cDNA amplicons. White, X-34 staining of Amyloid β plaque. Red, immunofluorescent staining of p-tau (AT8 primary antibody followed by fluorescent goat anti-mouse secondary antibody). **b**, The flowchart of the STARmap PLUS data analysis pipeline. **c**, Violin plot showing the accuracy (correct rate) of SEDAL sequencing for each FOV for all samples ($96.87\% \pm 5.00\%$). **d**, Histograms showing the ln-transformed number of transcripts (left) and genes (right) per cell in the 2,766-genes dataset before

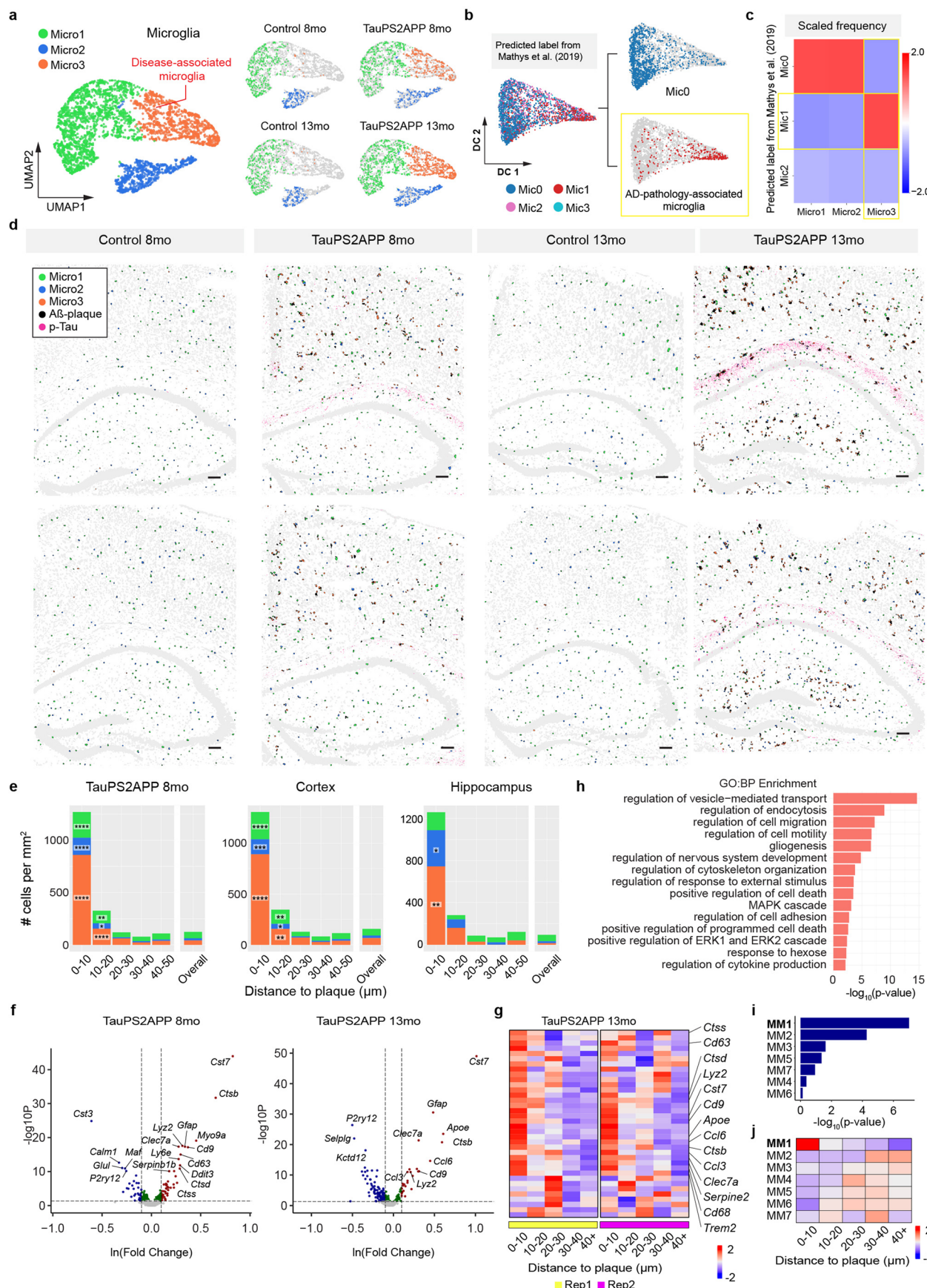
quality control. Red vertical lines represent median values. **e**, Histogram showing the number of transcripts after logarithmic transformation in the 2,766-genes dataset. Red vertical lines represent the filtering thresholds estimated by median absolute deviation (MAD). **f**, Number of transcripts and genes across samples. Violin plots showing the distribution of the number of reads per cell (top) and genes per cell (bottom) detected in each sample after quality control (N = 72,165 cells). Box plots depict the median (center) and interquartile range (IQR, bounds of the box), with whiskers extending to either the maxima/minima or to the median $\pm 1.5 \times$ IQR, whichever is nearest. **g**, Number of transcripts and genes across major cell types. Violin plots showing the distribution of the number of reads per cell (top) and genes per cell (bottom) detected in each major cell type (N = 72,165 cells). Box plots as in (f).



Extended Data Fig. 3 | See next page for caption.

Extended Data Fig. 3 | Classification and spatial distribution of major cell types. **a**, Dot plot showing the expression level of top five representative gene markers of each major cell type. **b**, Matrix plot showing the averaged expression level of canonical gene markers for each glial cell type of the 2,766-genes dataset. Values are normalized for each gene. **c**, Barplot showing the number of cells per cluster in Control and TauPS2APP mice. Data are represented as mean with 95% CI. Asterisks denote significant differences between Control and TauPS2APP ($n = 4$ samples per condition, two-sided $*P < 0.05$, t -test for two independent samples). **d**, Spatial atlas of top-level cell types in cortex and hippocampus regions of eight samples in the 2,766-gene dataset. Scale bars, 100 μm . **e**, Representative spatial distribution of cell-type compositions around A β plaque for TauPS2APP eight-month samples in both cortex and hippocampus. Stacked bar plot showing the density of each major cell type at different distance

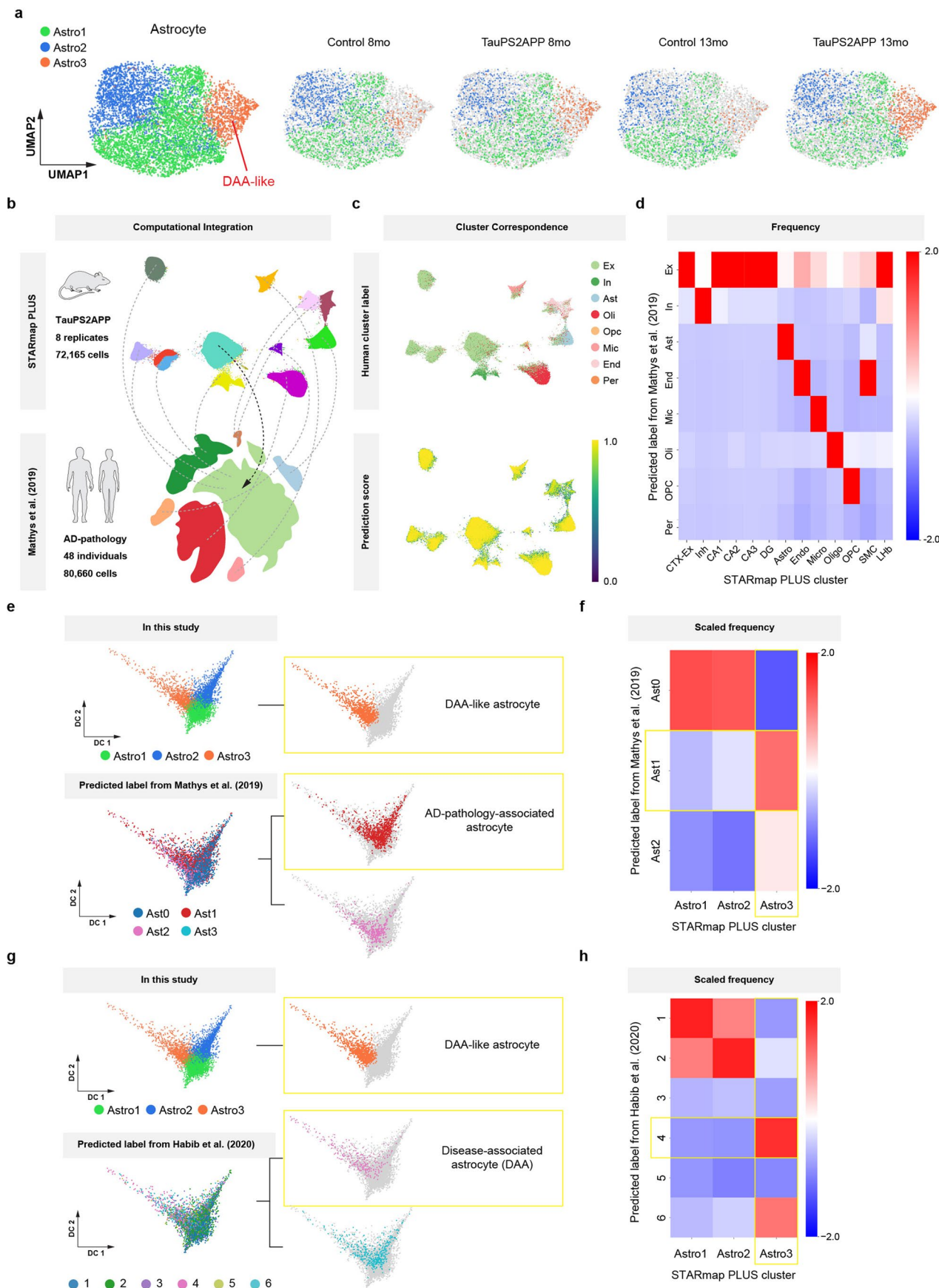
intervals to the A β plaque. The cell density of each major cell type in each area was included as the reference for comparison (overall). Asterisks denote significantly enriched cell types in each distance interval. One-sided one-sample t -Test, $*P < 0.05$, $**P < 0.01$, $***P < 0.001$, $****P < 0.0001$ vs. overall cell density. **f**, Cell-type composition around A β plaque at different distance intervals in both eight- and 13-month samples of the 2,766-gene dataset. Stacked bar plot showing the averaged density of major cell types in the cortex and hippocampus from different distance intervals around the A β plaque. The overall cell density of each cell type in each region was included as the reference for comparison (overall). Asterisks denote significantly enriched cell types in each distance interval. One-sided one-sample t -test, $*P < 0.05$, $**P < 0.01$, $***P < 0.001$, $****P < 0.0001$ vs. overall cell density.



Extended Data Fig. 4 | See next page for caption.

Extended Data Fig. 4 | Additional gene expression and spatial analysis of microglia. **a**, UMAP showing three subclusters of 3,732 microglia cells across different samples. **b**, Diffusion maps showing the subpopulation identified by predicted labels generated by the CCA integration with the astrocyte population from Mathys et al¹². Cells labeled as Mic0 and Mic1 from Mathys et al. were plotted separately for comparison. **c**, Heatmap showing the proportions (color bar, scaled per column) of microglia cluster IDs from Mathys et al¹². (rows) mapped to STARmap PLUS microglia subpopulations (columns). Cells were excluded if their label prediction score were less than 0.5. **d**, Spatial map of microglia subtypes in control and TauPS2APP samples. Scale bars, 100 μ m. **e**, Cell-type composition around A β plaque in different distance intervals for the TauPS2APP samples at eight months. Stacked bar plot showing the density of each microglia subpopulation in each distance interval around the A β plaque. Asterisks denote significantly enriched microglia subtypes in each

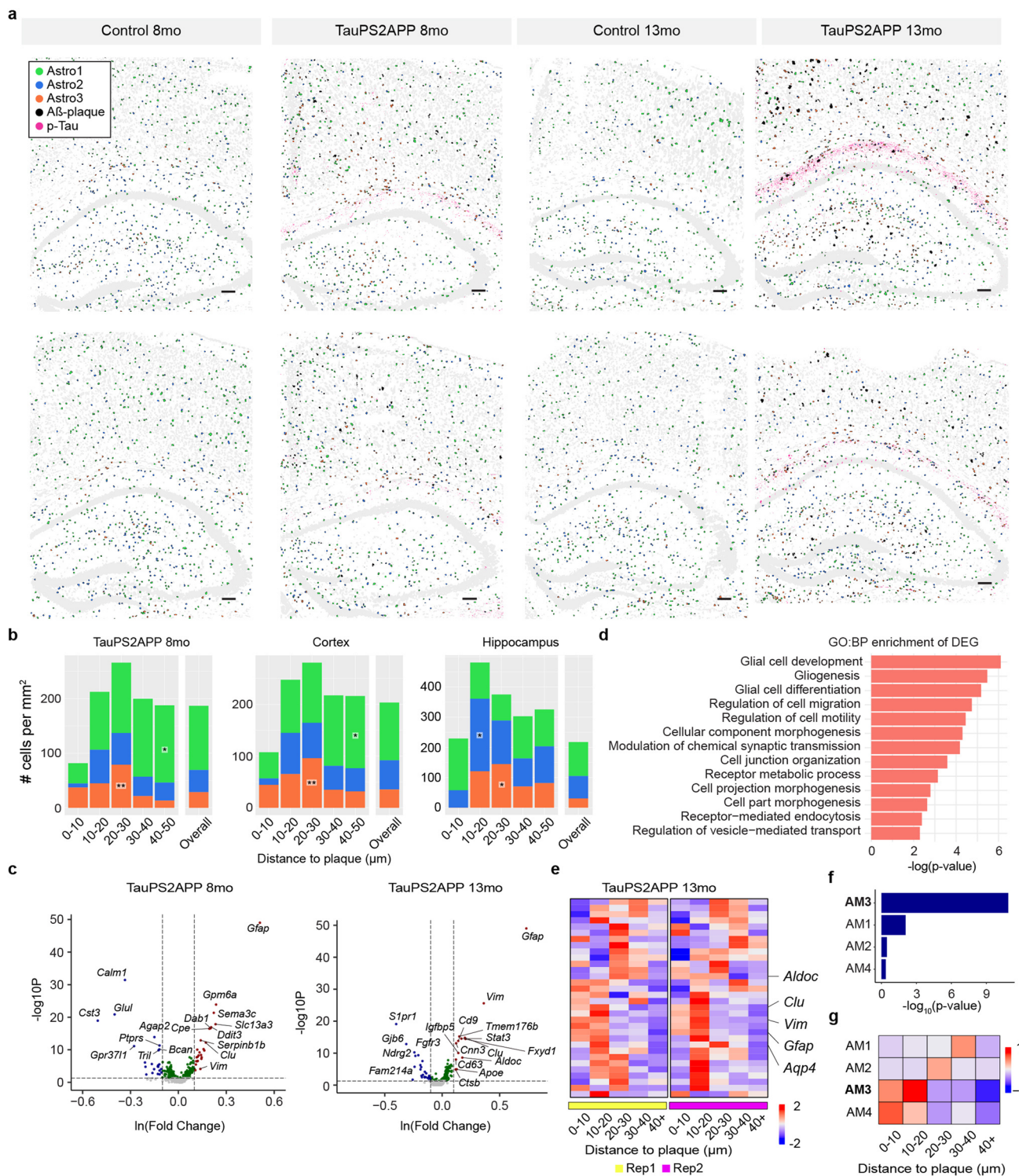
distance interval. One-sided one-sample t -test, * $P < 0.05$, ** $P < 0.01$, *** $P < 0.001$, **** $P < 0.0001$ vs. overall cell density. **f**, Volcano plots showing the differentially expressed genes (DEG) of microglia in TauPS2APP and control comparisons at eight- and 13-month time point (y-axis: -log adjusted p-value, x-axis: average log fold change). The two-sided Wilcoxon rank-sum test. Genes (p -value < 0.05 , absolute value of lnFC > 0.1) are marked in red (up-regulated) or blue (down-regulated). **g**, Matrix plot showing the z-scores of SDEGs of microglia across multiple distance intervals from plaques. **h**, Gene ontology enrichment analysis (Fisher's one-sided test) results of DEGs in microglia of the 13-month TauPS2APP samples. **i**, Barplots showing the DEG enrichment significance (the Chi squared test) of co-expression modules of microglia identified by scWGCNA. The gene module with the most significant DEG enrichment (MM1) is highlighted. **j**, Matrix plot showing the averaged z-score value of microglia gene modules across multiple distance intervals.



Extended Data Fig. 5 | See next page for caption.

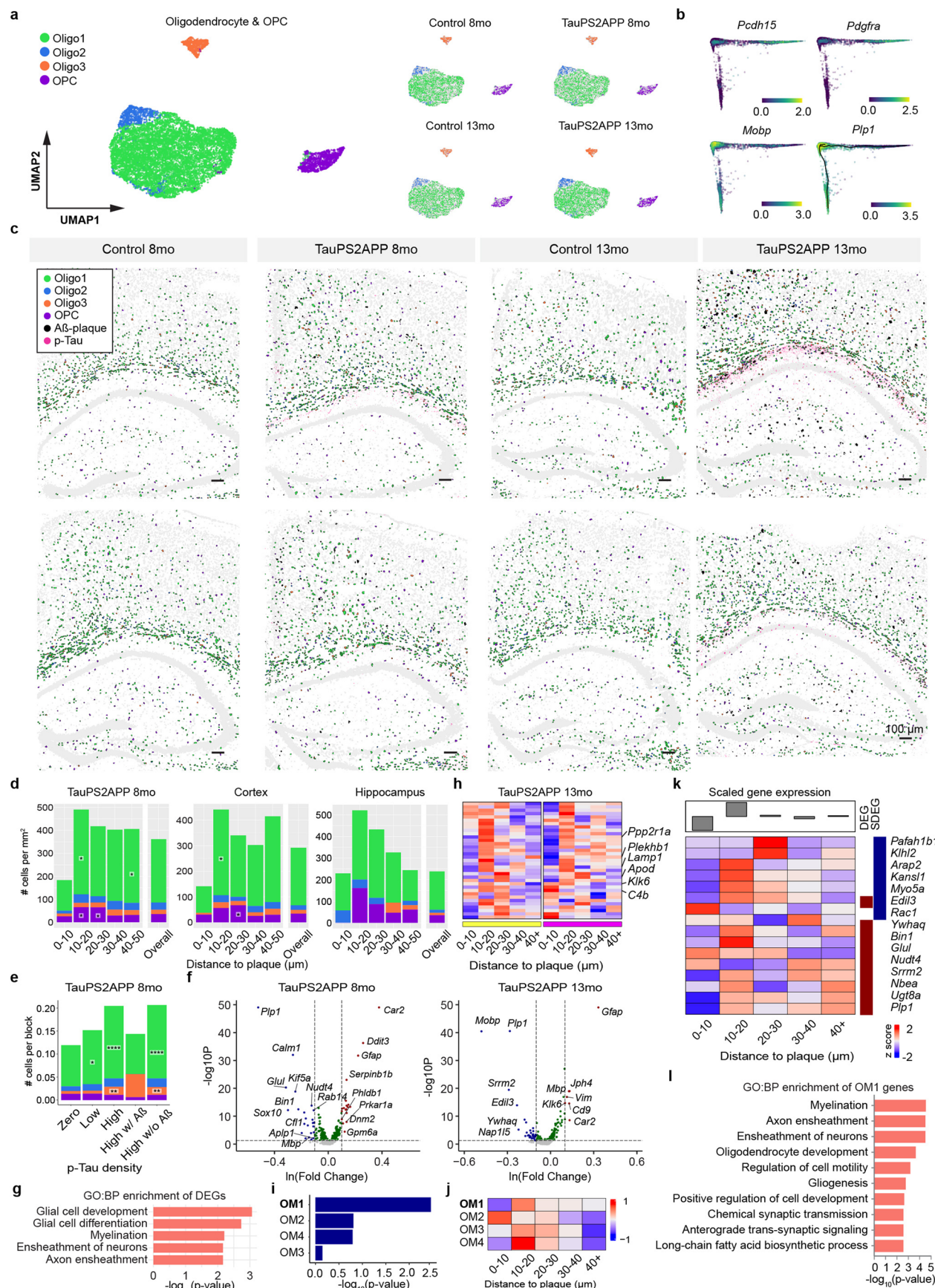
Extended Data Fig. 5 | Identification of disease-associated astrocyte populations in TauPS2APP mouse model through comparative studies with other AD mouse models and human patient samples. **a**, UMAP showing three subclusters of 6,789 astrocytes across samples. **b**, Schematic plot showing the basic idea of CCA integration and label transfer. In total, 72,165 cells from TauPS2APP and control mice were integrated with 80,660 cells from 48 human individuals with or without AD pathology in Mathys et al¹². **c**, UMAPs showing the predicted labels (top) and scores (bottom) of STARmap PLUS cells generated by the CCA integration with cells from Mathys et al¹². **d**, Heatmap showing the proportions (color bar, scaled per column) of cluster IDs from Mathys et al¹². (rows) mapped to STARmap PLUS cells (columns). Cells were excluded if their label prediction score were less than 0.5. **e**, Diffusion maps showing

the subpopulation identified by the present study (top) and predicted labels generated by the CCA integration with the astrocyte population from Mathys et al¹². (bottom). **f**, Heatmap showing the proportions (color bar, scaled per column) of astrocyte cluster IDs from Mathys et al. (rows) mapped to STARmap PLUS astrocyte subpopulations (columns). Cells were excluded if their label prediction score were less than 0.5. **g**, Diffusion maps showing the subpopulation identified by the present study (top) and predicted labels generated by the CCA integration with the astrocyte population from Habib et al⁹. (bottom). **h**, Heatmap showing the proportions (color bar, scaled per column) of astrocyte cluster IDs from Habib et al⁹. (rows) mapped to STARmap PLUS astrocyte subpopulations (columns). Cells were excluded if their label prediction score were less than 0.5.



Extended Data Fig. 6 | Additional gene expression and spatial analysis of astrocytes. **a**, Spatial map of astrocyte subtypes in control and TauPS2APP samples. Scale bars, 100 μm. **b**, Cell-type composition around Aβ plaque in different distance intervals for the TauPS2APP samples at eight months. Stacked bar plot showing the density of each astrocyte subpopulation in each distance interval around the Aβ plaque. The overall cell density of each subpopulation in each region was included as the reference for comparison. Asterisks denote significantly enriched astrocyte subclusters in each distance interval. One-sided one-sample *t*-test, **P* < 0.05, ***P* < 0.01 vs. overall cell density. **c**, Volcano plots showing the differentially expressed genes of astrocytes in AD and control comparison at eight and 13 months (y-axis: -log adjusted *p*-value, x-axis: average

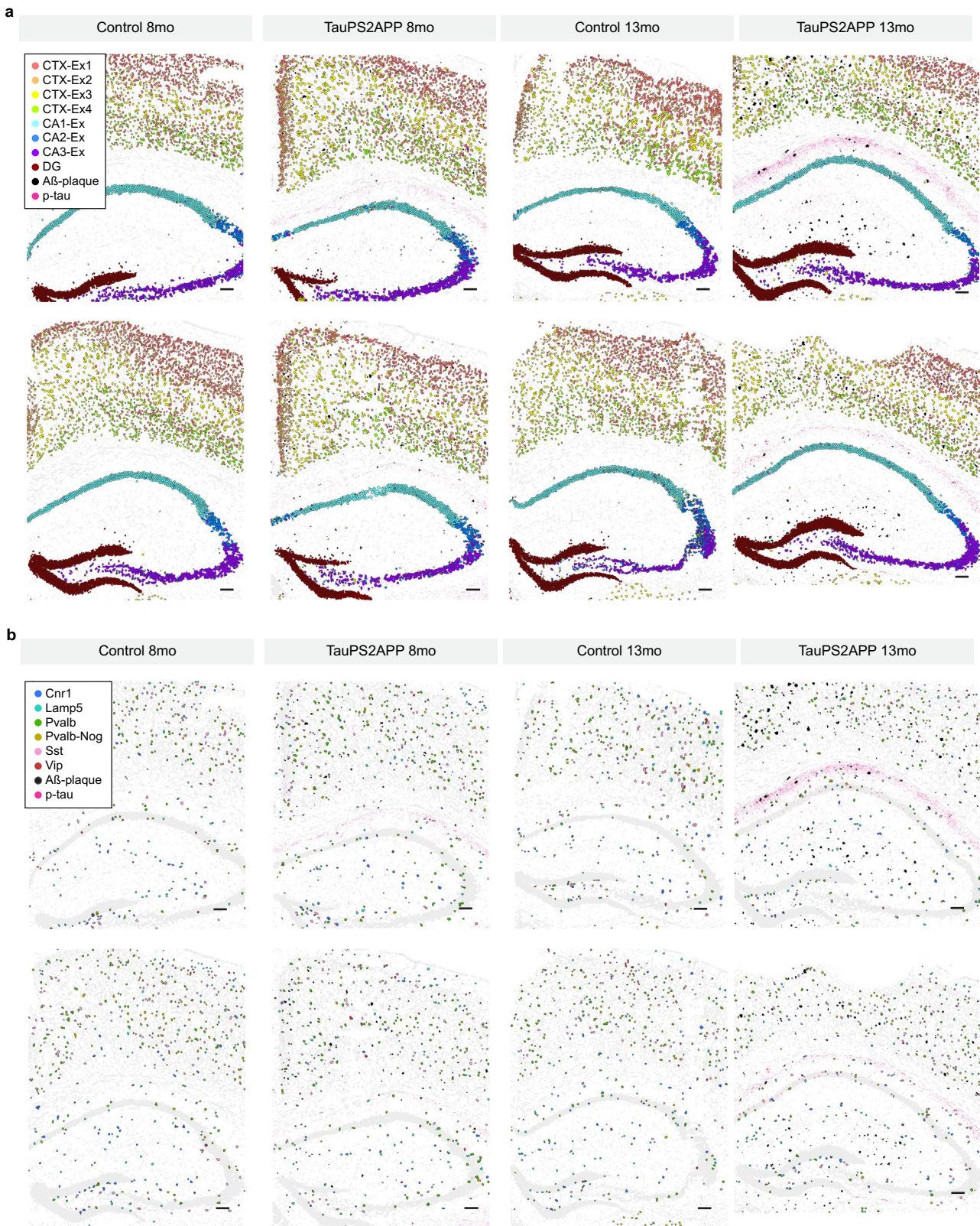
log fold change). The two-sided Wilcoxon rank-sum test. Genes (*p*-value < 0.05, absolute value of lnFC > 0.1) are marked in red (up-regulated) or blue (down-regulated). **d**, Gene ontology enrichment analysis (Fisher's one-sided test) results of DEGs in astrocytes of the 13-month TauPS2APP samples. **e**, Matrix plot showing the z-scores of SDEGs of microglia across multiple distance intervals from plaques. **f**, Barplots showing the DEG enrichment significance (the Chi squared test) of co-expression modules of astrocyte identified by scWGCNA. The gene module with the most significant DEG enrichment (AM3) is highlighted. **g**, Matrix plot showing the averaged z-score value of astrocyte gene modules across multiple distance intervals.



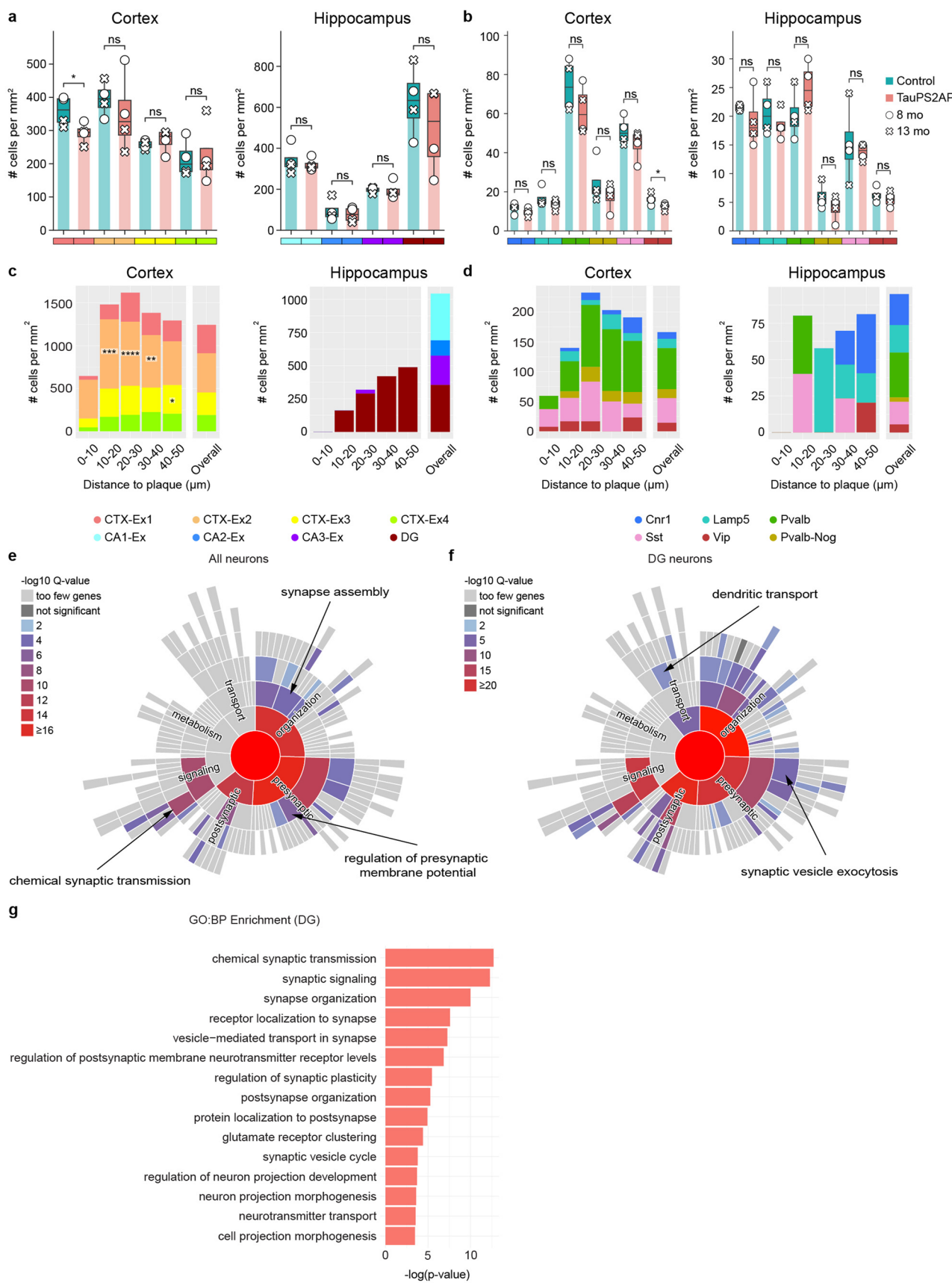
Extended Data Fig. 7 | See next page for caption.

Extended Data Fig. 7 | Additional gene expression and spatial analysis of oligodendrocytes and OPC. **a**, UMAP showing subclusters of 11,265 oligodendrocytes and 1,269 OPCs across samples. **b**, Diffusion map showing the normalized expression level of oligodendrocyte lineage marker genes in oligodendrocytes and OPCs. **c**, Cell-resolved spatial map for the oligodendrocyte and OPC population of control and TauPS2APP mice. Scale bars, 100 μ m. **d**, Cell type composition around A β plaque in different distance intervals for the TauPS2APP samples at eight months. Stacked bar plot showing the density of each oligodendrocyte subpopulation and OPC in each distance interval around the A β plaque. Asterisks denote significantly enriched oligodendrocyte subclusters and OPC in each distance interval. One-sided one-sample *t*-test, *P < 0.05 vs. overall cell density. **e**, Cell compositions in grid regions with different Tau positive pixel percentage of the TauPS2APP samples at eight months: zero (0%), low (50%), high (100%). One-sided one-sample *t*-test, *P < 0.05, **P < 0.01, ****P < 0.0001 vs. zero p-tau bin. **f**, Volcano plots showing DEGs of oligodendrocyte in AD and control comparison at eight and 13 months (y-axis:

-log adjusted p-value, x-axis: average log fold change). The two-sided Wilcoxon rank-sum test. Genes (p-value < 0.05, absolute value of lnFC > 0.1) are marked in red (up-regulated) or blue (down-regulated). **g**, Gene ontology enrichment analysis (Fisher's one-sided test) results of DEGs in oligodendrocytes of the 13-month TauPS2APP samples. **h**, Matrix plot showing the z-scores of spatial DEGs of oligodendrocytes across multiple distance intervals from plaques. **i**, Barplots showing the DEG enrichment significance (the Chi squared test) of co-expression modules of astrocyte identified by scWGCNA. The gene module with the most significant DEG enrichment (AM3) is highlighted. **j**, Matrix plot showing the averaged z-score value of astrocyte gene modules across multiple distance intervals. **k**, Matrix plot showing the z-scores of DEGs or SDEGs in the disease-associated gene module of oligodendrocytes in each distance interval around the A β plaque in TauPS2APP 13-month sample. The total averaged scaled expression level in different distance intervals was visualized by the bars on top of the matrix plots. **l**, Gene ontology enrichment analysis (Fisher's one-sided test) results of disease-associated gene module in oligodendrocytes.



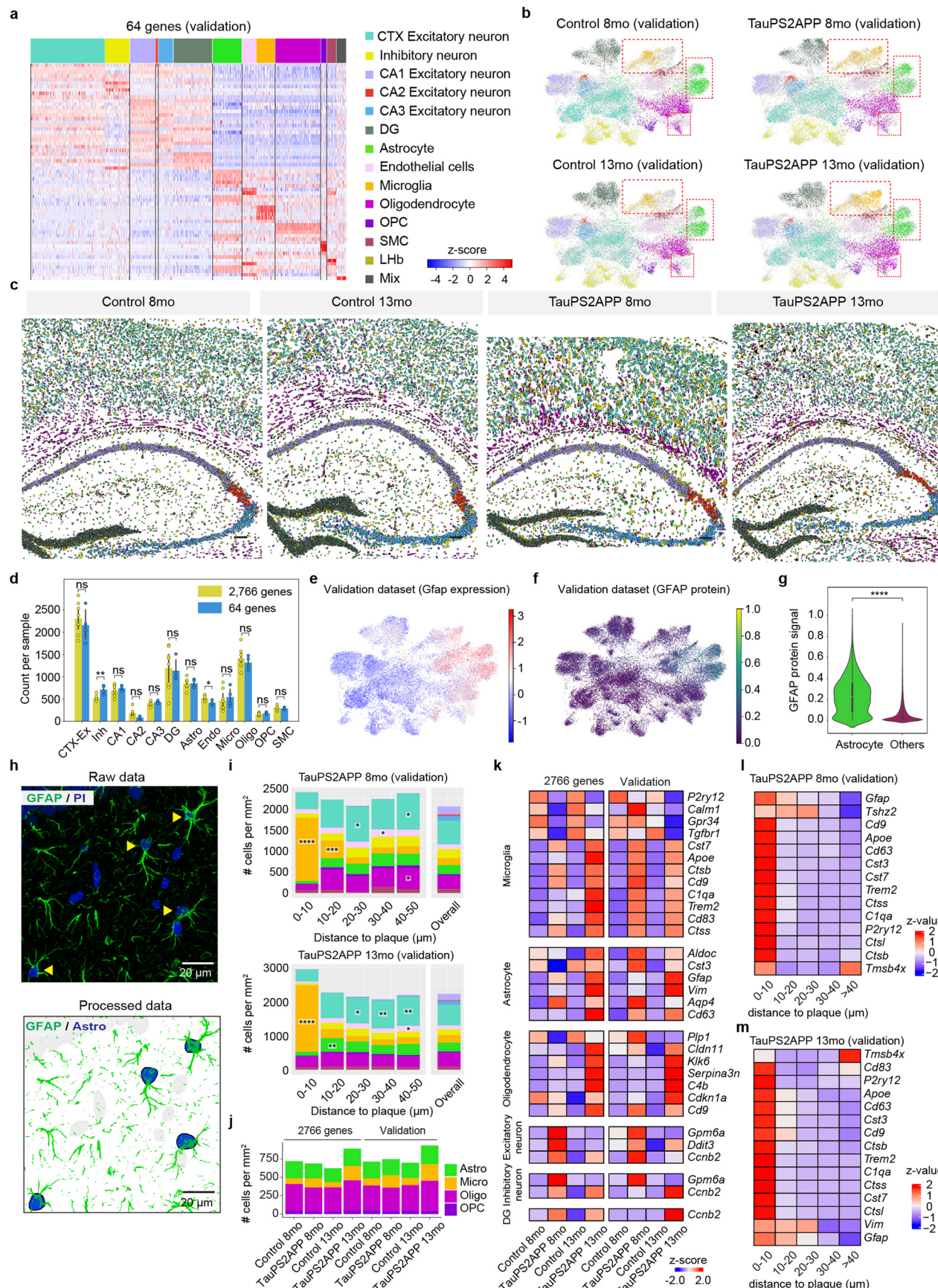
Extended Data Fig. 8 | Spatial maps for neuron populations of control and TauPS2APP mice. **a**, Cell-resolved spatial map for the excitatory neuron of control and TauPS2APP mice. Scale bars, 100 μ m. **b**, Cell-resolved spatial map for the inhibitory neuron population of control and TauPS2APP mice. Scale bars, 100 μ m.



Extended Data Fig. 9 | See next page for caption.

Extended Data Fig. 9 | Additional gene expression and spatial analysis of neurons. **a,b**, Boxplot showing the density (number of cells per mm²) of each excitatory neuron subcluster (**a**) and inhibitory neuron subcluster (**b**) in the cortex and hippocampus region in Control and TauPS2APP mice at two time points in eight independent samples. Box, 75% and 25% quantiles. Line, median. Dots or forks, individual samples. Student's *t*-test, one-sided *P < 0.05. **c,d**, Neuron composition around the plaque. Stacked bar charts showing the density (number of cells per mm²) of each subcluster of excitatory (**c**) and inhibitory (**d**) neuron population from different brain regions at each different distance intervals (0-10, 10-20, 20-30, 30-40, 40-50 μm) to the Aβ plaque from the cortex

and hippocampus region of TauPS2APP eight-month sample. The cell density of each subpopulation in each area was included as the reference for comparison (Overall). Asterisks denote significantly enriched neuron subclusters in each distance interval. One-sided one-sample *t*-test, *P < 0.05, **P < 0.01, ***P < 0.001, ****P < 0.0001 vs. overall cell density. **e,f**, Synaptic gene ontology term enrichment of DEGs (p-value < 0.05) identified in the TauPS2APP and Control comparison for all neuron population (**e**) and neurons in the dentate gyrus region (**f**) using SynGO. Color of the sunburst plot represents -log₁₀ Q-value at 1% FDR. **g**, Gene ontology enrichment analysis (Fisher's one-sided test) results of DEGs in dentate gyrus neurons of the 13-month TauPS2APP samples.



Extended Data Fig. 10 | See next page for caption.

Extended Data Fig. 10 | Validation of cell-type composition and spatial gene expression in TauPS2APP mice. **a**, Gene expression heatmaps for representative markers aligned with each top-level cell type of 64-gene (validation) datasets. Expression for each gene is z-scored across all genes in each cell. **b**, UMAP plot visualizing a non-linear dimensionality reduction for the transcriptomic profiles of 36,625 cells from four samples of the validation dataset. Cells are colored as in **(a)**. **c**, Spatial atlas of top-level cell types in cortex and hippocampus regions of four samples in the 64-gene dataset. Scale bars, 100 μ m. **d**, Barplot showing the number of cells per top-level cluster in 2,766-genes and 64-genes datasets. Data are represented as mean with 95% CI. Student's *t*-test, two-tailed * $P < 0.05$, ** $P < 0.01$. **e,f**, UMAPs showing the Gfap gene expression (**e**) and normalized GFAP protein signal (**f**) in 64-genes validation dataset. **g**, Violin plot shows the normalized GFAP protein signal level in the astrocyte cell population ($N = 3,423$ cells) compared to others ($N = 33,202$ cells). Box plots depict the median (center) and interquartile range (IQR, bounds of the box), with whiskers extending to the

maxima/minima or to the median $\pm 1.5 \times$ IQR. Two-sided *t*-test, **** $P < 0.0001$. **h**, Representative immunofluorescence images in the brain section of 64-gene validation samples ($N =$ four independent animals). Astrocytes were marked by yellow arrows in the raw data. **i**, Cell-type composition around A β plaque at different distance intervals in both eight- and 13-month samples of the 64-gene validation dataset. Asterisks denote significantly enriched cell types in each distance interval. One-sided one-sample *t*-test, * $P < 0.05$, ** $P < 0.01$, *** $P < 0.001$, **** $P < 0.0001$ vs. overall cell density. **j**, Barplot showing the cell density of astrocyte, microglia, oligodendrocyte and OPC in hippocampus alveus region in the 2,766-gene samples and validation samples. **k**, Matrix plot showing the row-wise scaled expression values of top significantly altered (rank by p-value) DEGs of glial cells and neuronal cells from TauPS2APP versus control samples. **l,m**, Matrix plot showing PIG that overlapped with 64-gene in each distance interval around the A β plaque in the eight-month (**l**) and TauPS2APP 13-month sample (**m**) of the 64-gene validation dataset. Colored by row-wise z-score.

Reporting Summary

Nature Portfolio wishes to improve the reproducibility of the work that we publish. This form provides structure for consistency and transparency in reporting. For further information on Nature Portfolio policies, see our [Editorial Policies](#) and the [Editorial Policy Checklist](#).

Statistics

For all statistical analyses, confirm that the following items are present in the figure legend, table legend, main text, or Methods section.

n/a Confirmed

- The exact sample size (n) for each experimental group/condition, given as a discrete number and unit of measurement
- A statement on whether measurements were taken from distinct samples or whether the same sample was measured repeatedly
- The statistical test(s) used AND whether they are one- or two-sided
Only common tests should be described solely by name; describe more complex techniques in the Methods section.
- A description of all covariates tested
- A description of any assumptions or corrections, such as tests of normality and adjustment for multiple comparisons
- A full description of the statistical parameters including central tendency (e.g. means) or other basic estimates (e.g. regression coefficient) AND variation (e.g. standard deviation) or associated estimates of uncertainty (e.g. confidence intervals)
- For null hypothesis testing, the test statistic (e.g. F , t , r) with confidence intervals, effect sizes, degrees of freedom and P value noted
Give P values as exact values whenever suitable.
- For Bayesian analysis, information on the choice of priors and Markov chain Monte Carlo settings
- For hierarchical and complex designs, identification of the appropriate level for tests and full reporting of outcomes
- Estimates of effect sizes (e.g. Cohen's d , Pearson's r), indicating how they were calculated

Our web collection on [statistics for biologists](#) contains articles on many of the points above.

Software and code

Policy information about [availability of computer code](#)

Data collection Leica LAS-X microscope imaging software was used during data acquisition. Huygens 20.10 was used for image deconvolution.

Data analysis MATLAB 2019b was used for imaging analysis of *in situ* sequencing images. Python 3.6 was used as a platform for some of the downstream analysis. StarDist python package was used for cell segmentation. Scanpy v1.4.6 was utilized for cell clustering. R (version 3.6.3) was used as another platform for rest of data analysis. EBImage v4.28.1 was utilized for processing of plaque and tau images. All *in-situ* single cell sequencing data was analyzed and visualized using Seurat v4.0.2. Pseudo-time analysis was performed by Monocle3 v0.2.1. Also ggplot2 v3.3.5 and ComplexHeatmap v2.7.10.9001 were utilized for data visualization. Fiji macro (ImageJ 1.53f51) was used for p-Tau images processing. gprofiler2 package v0.1.9, Cytoscape v3.9.1, EnrichmentMap v3.3.1, AutoAnnotation v1.3.3 and SynGO (<https://syngoportal.org/index.html>) were used for pathway related analysis. scWGCNA v1.0.0 R package was used for gene module analysis.

For manuscripts utilizing custom algorithms or software that are central to the research but not yet described in published literature, software must be made available to editors and reviewers. We strongly encourage code deposition in a community repository (e.g. GitHub). See the Nature Portfolio [guidelines for submitting code & software](#) for further information.

Data

Policy information about [availability of data](#)

All manuscripts must include a [data availability statement](#). This statement should provide the following information, where applicable:

- Accession codes, unique identifiers, or web links for publicly available datasets
- A description of any restrictions on data availability
- For clinical datasets or third party data, please ensure that the statement adheres to our [policy](#)

The STARmap PLUS sequencing data are available on Single Cell Portal (https://singlecell.broadinstitute.org/single_cell/study/SCP1375) and Zenodo (<https://doi.org/10.5281/zenodo.7332091>).

Human research participants

Policy information about [studies involving human research participants and Sex and Gender in Research](#).

Reporting on sex and gender	<input checked="" type="checkbox"/> This study did not include any human research participants.
Population characteristics	<input type="checkbox"/> See above.
Recruitment	<input type="checkbox"/> No human participants were recruited in this study.
Ethics oversight	<input type="checkbox"/> No study protocol related to human research participants was involved in this study.

Note that full information on the approval of the study protocol must also be provided in the manuscript.

Field-specific reporting

Please select the one below that is the best fit for your research. If you are not sure, read the appropriate sections before making your selection.

Life sciences Behavioural & social sciences Ecological, evolutionary & environmental sciences

For a reference copy of the document with all sections, see nature.com/documents/nr-reporting-summary-flat.pdf

Life sciences study design

All studies must disclose on these points even when the disclosure is negative.

Sample size	For 2,766-gene experiments, two 8-month TauPS2APP male mice, two 8-month WT male mice, two 13-month TauPS2APP male mice, and two 13-month WT male mice were used. For the 64-gene validation experiment, one 8-month TauPS2APP male mouse, one 8-month WT male mouse, one 13-month TauPS2APP male mouse, and one 13-month WT male mouse were used. No statistical methods were used to pre-determine sample sizes but our sample sizes are similar to those reported in previous publications.
Data exclusions	During the single cell transcriptomic analysis, cells with reads less than 41 or more than 680 were removed to exclude potential cell residues or under-segmented cell clusters.
Replication	All the major findings were validated in the second biological replicate.
Randomization	In each experimental batch, animals were chosen randomly based on their age. However, we matched transgenic Alzheimer's model TauPS2APP animals with WT non-transgenic littermate from the same mouse colony and age.
Blinding	For all samples received, the experimentalist did not acknowledge the sample identity (i.e. disease condition) until the experiment finished.

Reporting for specific materials, systems and methods

We require information from authors about some types of materials, experimental systems and methods used in many studies. Here, indicate whether each material, system or method listed is relevant to your study. If you are not sure if a list item applies to your research, read the appropriate section before selecting a response.

Materials & experimental systems

n/a	Involved in the study
<input type="checkbox"/>	<input checked="" type="checkbox"/> Antibodies
<input type="checkbox"/>	<input checked="" type="checkbox"/> Eukaryotic cell lines
<input checked="" type="checkbox"/>	<input type="checkbox"/> Palaeontology and archaeology
<input type="checkbox"/>	<input checked="" type="checkbox"/> Animals and other organisms
<input checked="" type="checkbox"/>	<input type="checkbox"/> Clinical data
<input checked="" type="checkbox"/>	<input type="checkbox"/> Dual use research of concern

Methods

n/a	Involved in the study
<input checked="" type="checkbox"/>	<input type="checkbox"/> ChIP-seq
<input checked="" type="checkbox"/>	<input type="checkbox"/> Flow cytometry
<input checked="" type="checkbox"/>	<input type="checkbox"/> MRI-based neuroimaging

Antibodies

Antibodies used

Phospho-Tau (Ser202, Thr205) Monoclonal Antibody (AT8), Biotin; Immunohistochemistry (IHC), ThermoFisher; Catalog # MN1020B; Clone: AT8; 1:100 dilution.
 Anti-GFAP antibody, Immunohistochemistry (IHC), abcam; Catalog # ab4674; 1:500 dilution.
 Goat anti-Mouse IgG (H+L) Cross-Adsorbed Secondary Antibody, Alexa Fluor 488; Immunohistochemistry (IHC), Thermo Fisher; Catalog # A-11001; 1:100 dilution.
 Goat anti-Chicken IgY (H+L) Secondary Antibody, Alexa Fluor 594; Immunohistochemistry (IHC), Thermo Fisher; Catalog # A-11042; 1:100 dilution.

Validation

Antibodies were chosen based on a literature review for each antibody to identify the best candidate for our experiments. Validation was determined by reviewing the manufacturer's literature, other published research, and prior experiments in the lab. Commercial antibodies were validated by the manufacturer:
 For anti-Phospho-Tau: <https://www.thermofisher.com/antibody/product/Phospho-Tau-Ser202-Thr205-Antibody-clone-AT8-Monoclonal/MN1020B>
 For anti-GFAP: <https://www.abcam.com/gfap-antibody-ab4674.html?productWallTab>ShowAll>

Eukaryotic cell lines

Policy information about [cell lines and Sex and Gender in Research](#)

Cell line source(s)	Human HeLa cell line used in this study was purchased from ATCC (CCL-2, lot 70016358).
Authentication	The cell line has been authenticated by the STR method.
Mycoplasma contamination	The cell lines were confirmed as mycoplasma negative by DAPI (4",6-diamidino-2-phenylindole) or Hoechst DNA staining and microscope imaging.
Commonly misidentified lines (See ICLAC register)	None.

Animals and other research organisms

Policy information about [studies involving animals; ARRIVE guidelines](#) recommended for reporting animal research, and [Sex and Gender in Research](#)

Laboratory animals	TauPS2APP: the pR5-183 line expressing the P301L mutant of human tau and PS2N141I and APPswe (PS2APP homo; P301L hemi), male, at the age of 8 months or 13 months. WT: no-transgenic pR5-183 line, male, at the age of 8 months or 13 months. Mice were group-housed up to 5 mice per cage in individually ventilated cages within animal rooms maintained on a 12:12-hour, light:dark cycle. Animal rooms were temperature and humidity-controlled, between 20-26°C and 30-70% respectively, with 10-15 room air exchanges per hour. Mice maintained on a regular chow diet.
Wild animals	The study did not include any wild animals.
Reporting on sex	The findings in this study applied to both sexes. Sex was considered in study design and we choose male mice for this study to decrease the influence of physiological parameters. Sex based analyses were not performed in this study as this mouse model had been used for a long time and no evidence showed that sex would influence the histopathology of the mice.
Field-collected samples	The study did not include any samples collected at the field.
Ethics oversight	All animal care and handling procedures were reviewed and approved by the Genentech IACUC and were conducted in full compliance with regulatory statutes, IACUC policies and NIH guidelines.

Note that full information on the approval of the study protocol must also be provided in the manuscript.